NOVA SCHOOL OF SCIENCE & TECHNOLOGY

DEPARTAMENT OF MATERIALS SCIENCES

HYDROXYAPATITE AEROGELS WITH PIEZOELECTRIC PARTICLES FOR BONE REGENERATION

Catarina Cunha Tavares

BSc in Micro and Nanotechnology Engineering

MASTER IN MICRO AND NANOTECHNOLOGY ENGINEERING

NOVA University Lisbon
September 2022

DEPARTAMENT OF MATERIALS SCIENCES

Hydroxyapatite aerogels with piezoelectric particles for bone regeneration

Catarina Cunha Tavares

BSc in Micro and Nanotechnology Engineering

Adviser: Maria Carmo Lança
Assistant Professor, NOVA University Lisbon

Co-advisers: João Paulo Borges
Associate Professor, NOVA University Lisbon

Examination Committee:

Chair: Pedro Miguel Cândido Barquinha
Associate Professor, NOVA University Lisbon

Rapporteurs: Marta Cristina Parracho Cançado Corvo
Researcher at the Department of Materials Science at NOVA University Lisbon

Adviser: Maria Carmo Lança
Assistant Professor, NOVA University Lisbon

MASTER IN MICRO AND NANOTECHNOLOGY ENGINEERING

NOVA University Lisbon
September 2022

Hydroxyapatite aerogels with piezoelectric particles for bone regeneration

ACKNOWLEDGMENTS

Gostaria de agradecer à minha orientadora Prof. Maria do Carmo Lança e coorientador Prof. João Paulo Borges por me terem aceitado como aluna de dissertação, pela introdução do tema e pelo apoio no decorrer deste projeto. Obrigado pelos desafios apresentados, bem como pelo que aprendi durante o projeto de dissertação.

Agradeço também ao DCM, CENIMAT e DF por todas as ferramentas e meios disponibilizados que tornaram possível a execução deste projeto.

Um obrigado à minha família, que ocasionalmente se esforça ao máximo para entender o que eu estudei nestes últimos anos, acabando por se esquecer uns meses depois, e especialmente pelas ofertas do forno nestes últimos meses, na esperança de me ajudar a gerir o tempo no laboratório.

Ao Pataco, André, Miguel, Claúdia, David e especialmente ao Guilherme, muito obrigada. A vossa companhia preencheu a minha vida académica com muita alegria e a ocasional história. Adorei estudar convosco, e, com o decorrer dos anos, adorei tentar estudar convosco, acabando por me distrair. Estudar é um privilégio por si só, mas poder partilhar essa parte da vida com vocês, tornou-a mais memorável.

ABSTRACT

Several materials have been researched to replace the damaged tissues or assist in the regeneration processes of the bone. New strategies for designing advanced functional biomimetic structures are continuously being reviewed and optimized. Advances not only on the chemical composition of the implants but also on their physical surface play an important role in enhancing the functionality of implants.
This dissertation focuses on the production of Hydroxyapatite (HAp) aerogels and aerogel composites of HAp with Barium Titanate ($BaTiO_3$) particles for bone tissue regeneration. The aerogels are composed of HAp nanowires (NWs) produced through solvothermal synthesis and later freeze dried.
All the commercially bought particles, 280nm, 2µm and 3µm, proved to contain $BaTiO_3$ in its tetragonal phase when characterized by an XRD, FTIR and Raman analysis. A thermal analysis (DSC and TGA) of the particles allowed to observe a shift in the phase of $BaTiO_3$, for the 280nm particles, around its Curie temperature, 130.6℃.
The product of the solvothermal reaction at a temperature of 180℃ for 18hours was verified to be carbonated Hydroxyapatite through a XRD and FTIR analysis. The aerogels with and without particles were observed with SEM, proving the existence of Hap wires, heterogeneous sized pores, as well as a good distribution of the $BaTiO_3$ particles.
The $BaTiO_3$ particles proved to be non-cytotoxic while the fabricated aerogels with and without particles were considered cytotoxic, however, the higher surface of the aerogels and easy dissolution may have altered the results.
In the assays of bioactivity assays, in SEM/EDS, difficulties were found when trying to differentiate between the apatite structures and the surface of the HAp wires. However, a quantitative EDS analysis shows that there is a possibly a cycle of CaP deposition followed by dissolution occurring.

Keywords: Piezoelectricity, Bone Tissue Regeneration, aerogel, hydroxyapatite, $BaTiO_3$, Barium Titanate, Solvothermal Synthesis.

RESUMO

Diversos materiais têm sido investigados de modo a substituir tecidos danificados ou auxiliar nos processos regenerativos do osso. Novas estratégias de modo a produzir estruturas biomiméticas funcionais avançadas são continuamente revisadas e otimizadas. Avanços não apenas na composição química dos implantes, mas também na sua superfície física, desempenham um papel importante em melhorar a funcionalidade dos implantes.

Esta dissertação dedica-se à produção de aerogéis de hidroxiapatite (HAp) e compostos de aerogel de HAp com partículas de Titanato de Bário ($BaTiO_3$) para regeneração do tecido ósseo. Os aerogéis são compostos por nanofios (NWs) de HAp produzidos por meio de síntese solvotérmica e posteriormente liofilizados.

Todas as partículas comerciais, 280nm, 2µm e 3µm, demonstraram a existência de $BaTiO_3$ em fase tetragonal quando caracterizadas por uma análise de DRX, FTIR e Raman. Uma análise térmica (DSC e TGA) das partículas permitiu observar uma mudança na fase do $BaTiO_3$ em torno de sua temperatura de Curie, 130.6 ℃, para as partículas de 280nm.

O produto da reação solvotérmica a uma temperatura de 180°C por 18 horas demonstrou ser hidroxiapatite carbonatada através de uma análise de DRX e FTIR.

Os aerogéis com e sem partículas foram observados no SEM, comprovando a existência de fios de Hap, poros de tamanhos heterogêneos, bem como uma boa distribuição das partículas de $BaTiO_3$.

As partículas de $BaTiO_3$ mostraram-se não citotóxicas enquanto os aerogéis fabricados com e sem partículas foram considerados citotóxicos, no entanto, a elevada área superficial dos aerogéis e fácil dissolução podem ter alterado os resultados.

Nos ensaios de bioatividade, encontrou-se dificuldade em diferenciar, no SEM/EDS, entre estruturas definidas de apatites e a superfície dos fios de HAp. No entanto, a análise quantitativa de EDS mostra que possivelmente existe um ciclo de deposição de CaP seguido de dissolução.

Palavras chave: Piezoeletricidade, Regeneração do Tecido Ósseo, aerogel, hidroxiapatite, $BaTiO_3$, Titanato de Bário, Síntese Solvotermal.

CONTENTS

LIST OF FIGURES

LIST OF TABLES

ABBREVIATIONS

BT	Barium titanate ($BaTiO_3$)
DSC	Differential scanning calorimetry
EDS	Energy Dispersive Spectroscopy
FTIR	Fourier-transform infrared spectroscopy
FWHM	Full width at half maximum
HAp	Hydroxyapatite
ICP-MS	Inductively coupled plasma mass spectrometry
NWs	Nanowires
SBF	Simulated body fluid
SEM	Scanning Electron Microscopy
TG	Thermogravimetric
XRD	X-Ray diffraction

SYMBOLS

β	Line broadening at half the maximum intensity (XRD)
θ	Degree (XRD)
π	Ratio of the circumference of a circle to its diameter, having a value rounded to eight decimal places of 3.14159265
r	Radius of a circle
τ	Average size of the crystalline grains
κ	Shape factor of the crystallite in the Scherrer equation
Δ	Relative uncertainty of the cell population
λ	Wavelength

1

INTRODUCTION

The bone is dynamic tissue capable of repair, growth, and remodelling in order to preserve its structural integrity and mineral homeostasis. Although bone tissue has a natural remodelling process, it has a threshold limit regarding how much can be regenerated. Fractures due to traumatic injuries, age degenerative processes or even surgical removal of tumors that result in absence or large defects of bone, led to the need of new ideas for biomaterials and medical devices to improve the natural healing process of the bone[1][2].

1.1 Biomaterials history

Biomaterials are defined, within the domain of health care, as a material engineered to interact with components of living systems in a way that assists any therapeutic or diagnostic procedure, for instance, evaluation, treatment, augmentation, repair or replacement of tissues or organs of the body[3][4].
Their history can be mainly classified into three generations, which will be mainly addressed regarding the area of hard tissue engineering. Bioinert materials are part of a first generation of biomaterials dating back to the 1960's. These types of materials are known for having a stable physiochemical property, meaning that, upon implantation of the material, there will not be a physiological reaction or immunological rejection by the body's tissue. However, it is important to note that no material is considered completely bioinert since all materials generate some kind of reaction after being implanted in the body. Examples of such are alumina and zirconia, which have been used for dental and orthopaedic applications due to their high strength, excellent corrosion and wear resistances, non-toxicity and in vivo biocompatibility. These materials, when implanted into the body, create a fibrous capsule around the material which isolates it from the surrounding tissue[3][5].
Contrary to the last generation, a second generation, focused on the interaction with the surrounding tissues, emerged in the 1980's. Bioactive materials have a positive effect on living tissues and bone regeneration, producing a specific response that starts to make a chemical bond between the material interface and the tissue. Thus, enhancing the biological response in the process of repair and reconstruction of hard tissues. Additionally, they could exhibit biodegradable properties, where the material is able to be broken down and degrade, due to their chemical structure, once in contact with the body tissue fluid. The chemicals produced during the resorption reaction should be able to be treated by the metabolic pathways of the body without any toxic effect. Therefore, one advantage is the fact that it would

not be required a secondary surgical procedure to remove the implanted material. Examples of bioactive and biodegradable materials are synthetic and natural polymers, calcium phosphates, calcium carbonate, and bioactive glasses[3][6][7].

More recently, a third generation of biomaterials, which actively supports and stimulates functional tissue regeneration, started to be more researched. This generation is manly designed to combine the bioactivity and degradability characteristics of the previous generation with improved osteoinductive properties. Osteoinduction is associated with both material composition and porosity, thus, the use of scaffolds with modified chemical surfaces, porous scaffolds seeded with bone marrow stem cells or loaded with biologically active substances and even scaffolds that respond to external stimuli by releasing specific previously mentioned therapeutic agents became a topic of interest[3][7][8].

1.2 Bone

In order to successfully design materials for bone-tissue engineering, it is of upmost importance to both understand the structure and composition of the bone and the cells responsible for bone remodelling process.

Bone is a composite material that consists of an organic component, composed primarily of collagen type I, and an inorganic mineral component, that serves as an ion reservoir. These ions form crystalline structures, in the form of nanorods of hydroxyapatite [$Ca_{10}(PO_4)_6(OH)_2$], surrounding and within the collagen microfibrils. While collagen fibbers allow for the flexibility properties of the bone, the addiction of a mineral inorganic phase ensure most of the stiffness. Therefore, the balance of both these properties is important and depends on the function each bone is required to provide, not being too flexible nor brittle[9][10].

The bone tissue can be classified into two distinct groups, cortical or trabecular, which present the same matrix composition, however, their structure, functionality and composition ratios within the bone differ. The cortical bone has a dense matrix mass, with a microscopic porosity of approximately 10% of total bone volume, surrounding the bone marrow and allowing for an higher compressive strength and contributing for the mechanical role of the bone, whereas the trabecular bone is imbedded into the bone marrow compartment and is constituted by a three-dimensional network of trabecular plates and rods which give an overall ‘spongy’ appearance with pores, making up to 50%–90% of the total trabecular bone volume and providing a surface area for blood vessels, bone marrow, and connective tissues to be in contact with the bone[9][11].

1.2.1 Bone remodelling process

Skeletal component cells mainly include osteoclasts, osteoblasts, osteocytes, bone lining cells, osteoprogenitor cells, chondrocytes, and their progenitor cells, bone marrow stem cells, that play different roles in the remodelling and maintenance of the bone tissue[1][9].

The bone remodelling cycle occurs in four sequential phases – activation, resorption, reversal and formation. Firstly, during the activation phase, osteoclast precursors differentiate into multinucleate osteoclasts. These precursors could be triggered either by systemic hormones, mechanical forces, or microscopic bone damage where osteocytes detect changes in bone fluid and release signals recruiting osteoclasts to remove the damaged bone. This stage is followed by the resorption phase where an osteoclast-

mediated bone resorption occurs. At the end of this phase, and beginning of the reversal phase, the resorption cavities contain a variety of mononuclear cells such as monocytes, osteocytes released from bone matrix, and preosteoblasts recruited to begin new bone formation. This phase consists of the transition between bone resorption and formation. Finally, during the formation phase, osteoblasts, responsible for building new bone tissue, synthetize new collagenous organic matrix, and regulate the mineralization of the matrix. Once the bone hardens, osteoblasts can become trapped inside, becoming known as an osteocyte. Thus, osteocytes are mature bone cells[2][9][12].
Many scientific studies are conducted in order to find scaffold designs and materials that promote bone regrowth in a shortened time limit. Therefore, the interactions between these natural remodelling processes and those scaffolds play an important role in the in the bone remodelling process.

1.3 Hydroxyapatite

1.3.1 Hydroxyapatite for bone regeneration

One material of interest is Hydroxyapatite, mostly represented by the chemical formula ($Ca_{10}(PO_4)_6(OH)_2$). This mineral belongs to the family of calcium phosphates and being an apatite, presents an Ca/P atomic ratio between 1.5 and 1.67. It is a highly biocompatible ceramic, chemically similar to that of the bone mineral phase, that demonstrates osteoconductive, osteoinductive and osteointegrative properties[13][14].
The main mechanism for bioactivity is the release of ionic products, such as calcium and phosphate ions, by partial dissolution upon implantation, which in turn leads to the precipitation of biological apatite on the surface of the ceramics in a process called bone mineralisation. With this in mind, an Hap surface, although not highly soluble, provides nucleation sites for the precipitation of apatite crystals, which in consequence contributes for the attachment of the implant to the living bone, improving implant fixation in the surrounding tissues[13][15].
Unfortunately, HAp bioceramics have shown to be brittle in nature and have low fracture toughness compared to the natural bone. Due to these mechanical properties, the applications of HAp are usual in orthopaedics as non-load bearing implants, filling of bone defects, or as coating, either dense or porous[16].

1.3.2 Hydroxyapatite Nanowire Aerogels

In the past decades, the design of HAp scaffolds has been researched in order to improve the properties previously mentioned. Apart from the chemical composition of the scaffolds, their morphology also plays an important role on the remodelling process of the bone and osteointegration of the implant[5].
For instance, porosity of a scaffold, controlled by its synthesis method, is shown to improve implant performance due to better bio-integration and mechanical stability of the implant. The higher surface area and open pore structure improve the transport of gas and nutrients along an higher surface area and allow the diffusion of cells responsible for the bone tissue deposition[14][17]. It was studied that the optimal size of the pores varies for specific cells and tissues. For example, 200–400 μm sized pores were found to be suitable for bone tissue formation, whereas 50–200 μm pores were better for smooth muscle

cell growth. Additionally, scaffolds with pore sizes between 10-44 and 44–75 μm enable accommodation of only fibrous tissue[8].
It is important to note that the increase of porosity exponentially decreases the resistance to mechanical loads. However, the mechanical properties of a material can be improved by changing the porous sizes and its distribution. Studies have shown that larger pore sizes and homogeneous size distribution of pores reduce the resistance to mechanical stress, while heterogeneous pore sizes proved to show higher resistance[17]. Among various morphologies of HAp, Hydroxyapatite nanowires (HAp NWs) seem to be very promising in several fields. Gao-Jian Huang, explored the use of highly porous aerogels (~99.7%) composed of HAp NWs as scaffolds in bone regeneration and neovascularization. Compared to solid HAp ceramics, the HAp NWs aerogels promoted the adhesion and spreading of osteoblasts and other cells responsible for bone defect repair deeply into the pores, while exhibiting better mechanical properties, such as high elasticity and high fracture resistance due to the flexibility and network of the HAp nanowires[18][19].

1.4 Piezoelectricity

The piezoelectric effect is an intrinsic property of some materials whereby an electrical polarity is produced when mechanical force is applied on the material. In addition, a converse piezoelectric effect is also observed when the material exhibits stress, upon an applied electrical field[20].
As early as 1957, Eiichi Fukada et. al, developed research that proved the existence of piezoelectric effect in bone. The specimens observed were cut from the femur of a man and ox. The piezoelectric effect is only observed when shearing force is applied to the collagen fibres to make them slip past each other. This increased the interest in recreating these piezoelectric responses in bioactive implants, mimicking the electrical behaviour of the bones[21].
There are several studies, in vitro and in vivo, that prove the correlation between charged scaffolds and regeneration properties of the bone. Either by evaluating the formation of calcium phosphate (CaP), related to the mineralization process during the formation of new bone, or the attachment and proliferation of osteoblast and other osteogenic cells on charged surfaces[22-26].

1.4.1 $BaTiO_3$

Barium Titanate (BT) is a perovskite ferroelectric ceramic with interesting applications in the biomedical field as it is not only biocompatible, but also demonstrates piezoelectric properties[27].
Ferroelectrics constitute a subgroup of piezoelectric materials, characterized by the presence of a spontaneous polarization in the unstrained state and the capability to reorientate in the direction of polarization. This characteristic originates from the formation of an electrical dipole due to an asymmetric distribution of ions in certain crystal structures[20].
At high temperatures, BT exhibits a cubic structure, as in Figure 1 a), with Ba^{2+} cations at the corner sites of the unit cell, a smaller Ti^{4+} cation in the center and face centered oxygen O^{2-} ions. At temperatures below the Curie Temperature, Ti atom will suffer an off-center displacement toward one of the O atoms, transforming the unit cell of BT into a tetragonal structure that shows asymmetry, such as in

Figure 1 b) and c), resulting in an electrical dipole that is responsible for the piezoelectric behaviour[28][29].

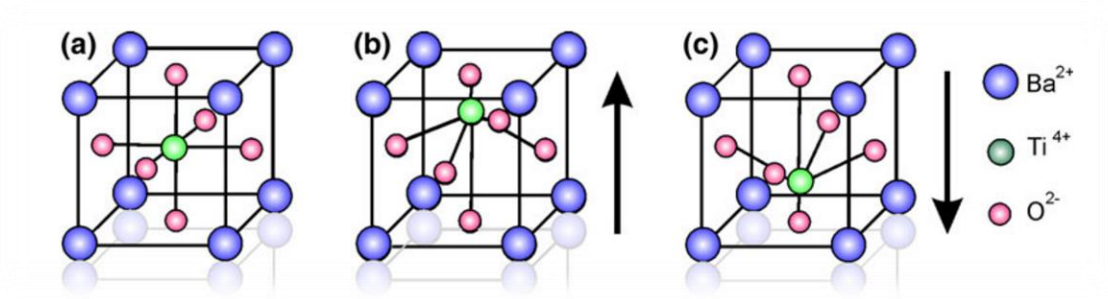

Figure 1. a) The cubic and symmetrical perovskite unit cell for BaTiO3, b) and c) The tetragonal perovskite unit cell with formation of a dipole by displacement of the Ti4+ ion[20].

As previously mentioned, this behaviour seems rather interesting as a stimulus for bone remodelling, possibly enhancing the osteocondution effects of a scaffold.

The main purpose of this work will be the production of hydroxyapatite aerogels and composite aerogels of hydroxyapatite embedded with barium titanate particles for biomedical applications in hard tissue regeneration. All the $BaTiO_3$ particles and the aerogels will be tested for cytotoxicity as well as characterized by thermal analysis (DSC and TGA), XRD, FTIR and Raman. The HAp aerogels will be analyzed by SEM to make sure that the pore size and interconnectivity of pores is suitable for its applications. In addition, the dispersion of the $BaTiO_3$ particles will be observed on the composite aerogels. Finally, the bioactivity of the aerogels with and without particles will be studied through SBF immersion.

The fabrication of the composites with $BaTiO_3$ particles may allow future studies to evaluate the influence of polarized surfaces, as a stimulus for bone reparation.

2

MATERIALS AND METHODS

2.1 Sample synthesis

2.1.1 Hydroxyapatite nanowire synthesis

The HAp NWs were synthesized based on previous research by Zhi-Chao Xiong, et al[19]. Firstly, 13.50g of deionized water, 4.75 g of methanol, and 9.36 g of oleic acid (OA) were mixed under mechanical stirring. Secondly, three solids were dissolved in deionized water and poured separately into the above mixture. The first solution consisting of 15 ml of NaOH with 6.54 weight/weight% (w/w%) concentration, was poured and stirred for 30 min, while the other solutions of 12 ml of $CaCl_2$ with 2.70w/w% and 18ml of $NaH_2PO_4.2H_2O$ with 4.94w/w%, were poured and stirred for 10 min each. Finally, 5ml of the reaction system was poured into a 100 mL Teflon-lined stainless-steel autoclave for a solvothermal reaction. This reaction was tested for different times such as 5, 7, 18 and 24 hours at different temperatures 120℃, 165℃ and 180℃. The resulting slurry was stirred for 30 min at 300 rpm. In order to separate the HAp NWs from the impurities, the slurry was centrifuged for 10 min at 3000rpm and washed with progressively diluted methanol/deionized water ratios. The HAp NWs were stored in deionized water.

2.1.2 Aerogel synthesis

To produce HAp aerogels, part of the NWs slurry was put into a cell culture plate of 24 wells, used as a mold, and frozen at -5 °C for 12 h, followed by lyophilization at 0.01 ℃ and 611.2 Pa for 24 h.
In order to produce HAp aerogels with $BaTiO_3$ (BT), the particles with sizes of 280 nm (LT#NG04MO0503), 2 µm (LT#MKBB0111V) and 3 µm (LT#MFCD00003447), were dispersed in the remaining HAp NWs slurry, corresponding to 20BT/80HAp ratio of weight percentage, dispersed through sonication for 15 min and lyophilized in the same conditions.

2.2 Sample characterization

2.2.1 Chemical and stuctural characterization.

An analysis of the $BaTiO_3$ and HAp crystallographic structure was conducted in a X'Pert PRO (PAN-Alytical) X-ray diffractometer with the use of CuKα radiation generated at 45 kV and 40 mA, in the range of $10°<2\theta<90°$, with a step size of 0.08°. For the $BaTiO_3$, in order to better observe the phase composition of the sample, an additional analysis was conducted in the range of $44°<2\theta<47°$, with a step size of 0.002°. The obtained diffraction peaks were compared with International Centre for Diffraction Data (ICDD) sheet for tetragonal $BaTiO_3$ #00-005-0626, cubic $BaTiO_3$ #01-084-9618 and $Ca_{10}(PO_4)_6(OH)_2$ #046-0905, and with with JCPDS cards for $CaCl_2$ #26-1053, $NaH_2PO_4•2H_2O$ #10-0198 and NaOH #35-1009.

Additionally, a Fourier-transform infrared spectroscopy (FTIR) analysis with the use of the spectrophotometer FT-IR Thermo Nicolet 6700, was carried out with wavenumbers from 4000 cm^{-1} to 400 cm^{-1}, to identify the functional groups of $BaTiO_3$ and HAp.

To evaluate the molecular structure of the samples and additionally confirm the existence of a tetragonal phase of the $BaTiO_3$, a Raman spectroscopy analysis was conducted using the Renishaw inVia Qontor micro-Raman spectrometer. 5 scans were made, each with an integration time of 1 second, using an incident 632.81 nm laser with an intensity of 0.32 mW and a frequency range from 150 cm^{-1} to 1000 cm^{-1}.

2.2.2 DSC/TG

To better evaluate the phase present in the $BaTiO_3$ particles and its magnetic properties, the Curie temperature was measured by differential scanning calorimetry (DSC), heating the samples from 20 °C to 250 °C at a 5 °C min^{-1} rate using DSC 204 F1 Phoenix from NETZSCH.

2.2.3 SEM/EDS

To ensure the existence of HAp nanowires, the aerogel's morphology and the dispersion of the $BaTiO_3$ particles along them, the samples were morphologically observed under a scanning electron microscope/Energy Dispersive X-ray Spectrometry (SEM/EDS), by the model Hitachi TM 3030Plus. All samples were sputter-coated with either gold or titanium before SEM observation.

2.2.4 Cytotoxicity analysis

The colorimetric cytotoxicity assays were performed on all the $BaTiO_3$ particles and HAp aerogels with and without $BaTiO_3$, with the use of resazurin, in conformity with the standard ISO-10993 "Biological evaluation of medical devices, Part 5: Tests for in vitro cytotoxicity" test protocol, described in Annex A I. When in contact with metabolic active cells, resazurin which shows a non-fluorescent blue coloration, is reduced to a fluorescent pink compound denominated resorufin. The absorbance spectrum of each well was measured in a Biotek ELX800 microplate reader at 570 nm and 600 nm, corresponding to the absorbance maximum of resazurin and resorufin, respectfully. Then, viability of the cells was

evaluated by calculating the absorption spectrum of each well relative to a control medium, where the variation of the absorbance is proportional to the number of metabolic active cells.
For the absorbance values measured, the relative population of the cells was calculated according to:

$$\mathrm{P}(\%) = \frac{Act}{Acc} \times 100 \quad 2.1$$

Where Act is the average absorbance of a sample at 600cm subtracted from the average absorbance at 570 nm and Acc is the average absorbance of the negative control group at 600 nm subtracted from the average absorbance at 570 nm. The standard deviation of the absorbance in the sample medium, ΔAct, and control groups, ΔAcc, was also calculated.
The Relative uncertainty of the cell population, Δ, was calculated by the propagation of uncertainty:

$$\Delta = P \times \sqrt{\left(\frac{\Delta Act}{Act}\right)^2 + \left(\frac{\Delta Acc}{Acc}\right)^2} \quad 2.2$$

2.2.5 Bioactivity analysis

The bioactivity of the HAp aerogels with and without $BaTiO_3$ was analyzed by evaluating the growth of Ca-P structures on the surface of the membrane when in contact with simulated body fluid (SBF) serum. The protocol followed for preparing the SBF solution was based in current methods[30][31] and can be found in Annex A II.
The minimum volume of SBF to aerogel surface area was calculated following the proportion present in equation 2.3 [31] where SA is the Surface Area, V is the Solution Volume and 0.1 is in cm^{-1}:

$$0.1 = \frac{\mathrm{SA}}{\mathrm{V}} \quad 2.3$$

The evaluated samples consist of a Hap aerogel without particles, three Hap aerogels with $BaTiO_3$, each with different particle sizes and a control group which was not in contact with the SBF. Each sample was submerged for 1, 3 and 7 days and the SBF solution was renewed every 2 days. Finally, the samples were observed in SEM and EDS to identify the growth of Ca-P structures.

3

RESULTS AND DISCUSSION

This chapter is divided into the characterization of the $BaTiO_3$ particles, HAp NWs and finally, the characterization of the HAp aerogels, both with and without $BaTiO_3$ particles.

3.1 Barium Titanate

3.1.1 X-ray Powder Diffraction (XRD) analysis

The XRD diffractogram shows the diffraction peaks of $BaTiO_3$ measured for different particle sizes: 280 nm, 2 µm, 3 µm and was carried out in order to confirm the existence of a tetragonal phase $BaTiO_3$. The comparison of the peaks with the ICDD data sheet #00-005-0626 and #01-084-9618, corresponding to tetragonal and cubic $BaTiO_3$, respectively, confirmed that the diffraction spectrum in Figure 2 a) was characteristic of Barium Titanate in a tetragonal phase, with no additional impurity peaks.

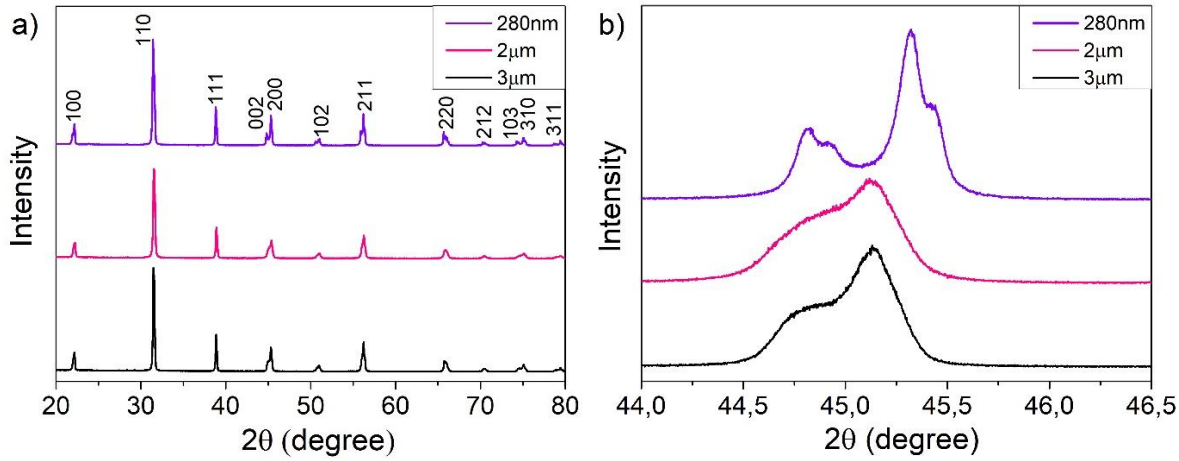

Figure 2. XRD analysis of the $BaTiO_3$ powders with diffraction angles a) from 10º to 90º and b) from 44º to 47º.

According to both data sheets, the transformation from a cubic to a tetragonal $BaTiO_3$ phase exhibits itself in the XRD spectrum as the presence of double peaks along the diffraction pattern due to the asymmetry of the unit cell[32].

This could be seen in further detail in Figure 2 b), where the existence of a split peak around 45º distinguishes tetragonal $BaTiO_3$ from its cubic phase. The double diffraction peak is more visible on the 280nm powders, with a peak at 44.8° and 45.4° corresponding the planes (002) and (200), respectively. Regarding the 2 µm and 3 µm powders, there is a similarity between the intensity of the diffraction split, also corresponding to the same planes. Since the less noticeable splitting could exist due to the large peak widths, caused by larger crystallite sizes, the average size of the crystalline grains, τ, present in Table 1, were calculated according to the Scherrer equation 3.1, using a X-ray wavelength of $\lambda(CuK\alpha) = 1.5418\times10^{-10}$ m, a shape factor of the crystallite, κ, of 0.9 and a line broadening at half the maximum intensity, β, for each peak[33].

$$\tau = \frac{\kappa\lambda}{\beta\cos\theta} \qquad 3.1$$

Table 1. Crystallite size of each $BaTiO_3$ sample according to the Scherrer equation.

Sample	Peak, 2θ (°)	FWHM, β (rad)	Crystallite Size, τ (nm)
280 nm	31.43	4.81×10^{-3}	29,90
2 µm	31.54	4.42×10^{-3}	32.54
3 µm	31.49	3.90×10^{-3}	36,88

It can be seen that the average crystallite sizes are larger for the micrometric samples, 2 µm and 3 µm, leading to larger, less defined peaks and a bigger superposition between each other.
Although all the samples seem to exhibit a tetragonal-dominant structure, the samples of 2 µm and 3 µm show a smaller difference between the angles corresponding to the two peaks in Figure 2 b), when compared to the sample of 280 nm, which is caused by a reduced tetragonal phase and the partial existence of a cubic phase. A higher percentage of tetragonal phase, such as in the particles of 280 nm, would be more suited for a possible polarization of the HAp aerogels[32][34].

3.1.2 Fourier-transform infrared spectroscopy (FTIR) analysis

Complementary the XRD spectroscopy structural analysis, FTIR spectrum of the commercial $BaTiO_3$ particles, was obtained at room temperature from a wavenumbers of 4000 cm^{-1} to 400 cm^{-1}, allowing to identify the present functional groups of $BaTiO_3$.
The observed FTIR spectrum on Figure 3, taken in transmittance mode, exhibits a small peak at 438 cm^{-1} and a wide peak around 540 cm^{-1} indicating the existence of a Ti-O bond, characteristic of $BaTiO_3$[35]. Moreover, vibrational bands signaled at 860 cm^{-1} and 1450 cm^{-1} are compatible to bending vibrations of a C-O bond which could be linked to the reagents used for the fabrication of the commercial particles, for instance, barium carbonate. Finally, the bands around 3000 cm^{-1} correspond with the presence of an OH group from the H_2O content in the samples[32].

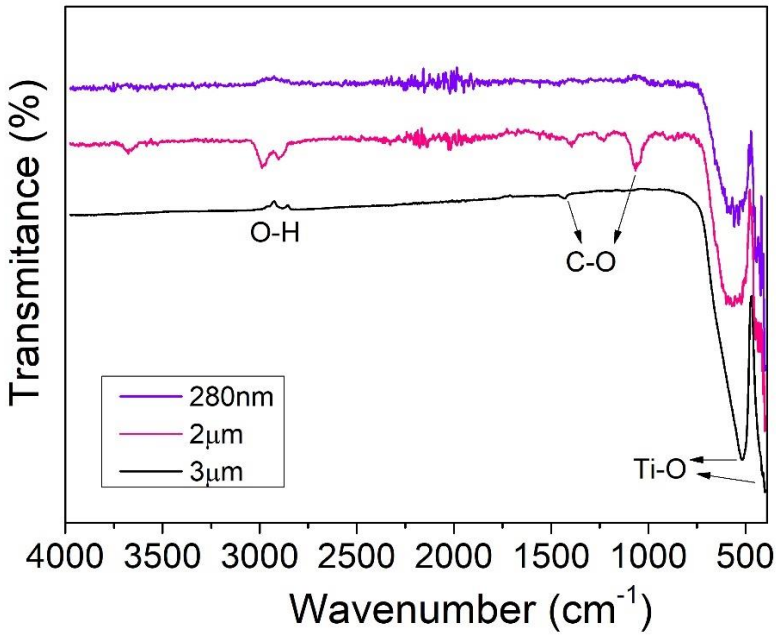

Figure 3. FTIR spectrum of 280nm, 2μm and 3μm $BaTiO_3$ particles, taken in transmittance mode.

3.1.3 Raman spectroscopy analysis

In order to confirm further confirm the existence of a tetragonal phase of the powders, an analysis of the powder's Raman spectroscopy was used.

A molecule of $BaTiO_3$ contains five atoms, leading to 12 optical vibrational modes. Based on the crystallography, Raman-active modes for tetragonal $BaTiO_3$ are four E(TO + LO), three A_1(TO + LO) and a B_1(TO + LO), while no Raman-active mode is predicted for the cubic phase due to the isotropic distribution of electrostatic forces surrounding Ti^{4+} ions[36]. Accordingly, the Raman spectrum presented in Figure 4 is typical of a nonsymmetric structure.

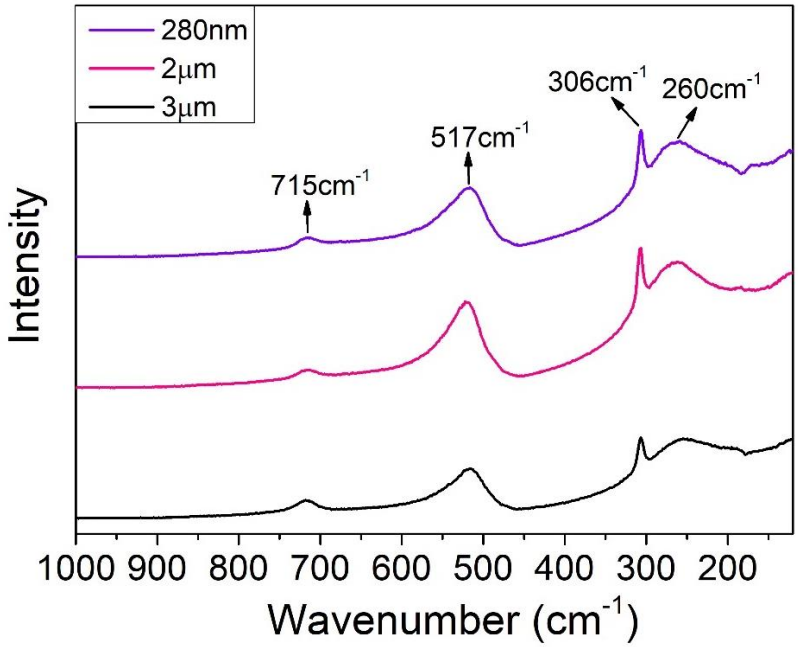

Figure 4. Raman spectroscopy of $BaTiO_3$ particles sizes 280 nm, 2 μm, 3 μm.

In the case of the represented Raman spectra, there can be identified four dominant Raman band positions centered near 260 cm^{-1}, 306 cm^{-1}, 517 cm^{-1} and 715 cm^{-1}, indicating the presence of the tetragonal phase.

Since more than one phonon modes are available for each Raman band and the reported wavenumbers of some A_1 and E modes are very close to each other, the observed modes are mixed. As literature suggests, the broad Raman band near 260 cm^{-1} corresponds to a Raman mode $A_1(TO_2)$ and a band near 306 cm^{-1} is assigned to the B_1 and E(TO + LO) modes, suggesting an asymmetric vibration of the $[TiO_6]$ octahedra. In addition, the band at 517 cm^{-1} is related to the $A_1(TO_3)$ and E(TO) modes, while a Raman band around 715 cm^{-1} is corelated with the A_1(LO) and E(LO) mode[32][37].

Accordingly, the Raman results clearly show that all $BaTiO_3$ samples possess a distortion of the $[TiO_6]$ octahedra and consequentially, ferroelectric properties[32]. It can be concluded that the XRD data corresponds to the obtained Raman spectrum, confirming the existence of a tetragonal phase in all the samples.

3.1.4 Differential scanning calorimetry and Thermogravimetric (DSC/TG) analysis

The DSC/TG measurements were made after the chemical studies, mentioned previously, in order to understand the temperature evolution at which the $BaTiO_3$ structural transformation takes place from tetragonal phase to cubic.

An endothermic peak was to be expected around 120 °C, corresponding to the Curie Temperature of $BaTiO_3$, where a transition from tetragonal to cubic phase occurs[38]. However, it could be noted in Annex B III, Figure B 1 and Figure B 2, an absence of endothermic peaks in the 25 ºC to 200 ºC temperature range for both the 2μm and 3μm samples. Only in the case of the 280nm sample, shown Figure

5, there is a peak at 130.6 ºC, suggesting the previously mentioned phase transition. In regard to the thermogram plot, there was little mass change in the tested temperature range for all samples.
Since the chemical analysis confirmed the existence of $BaTiO_3$, the lack of characteristic peaks could stem from the lack of resolution of the equipment used in the chosen measurement range. The use of an equipment with higher resolution in a smaller temperature range could allow for a better examination of the material's thermal properties.

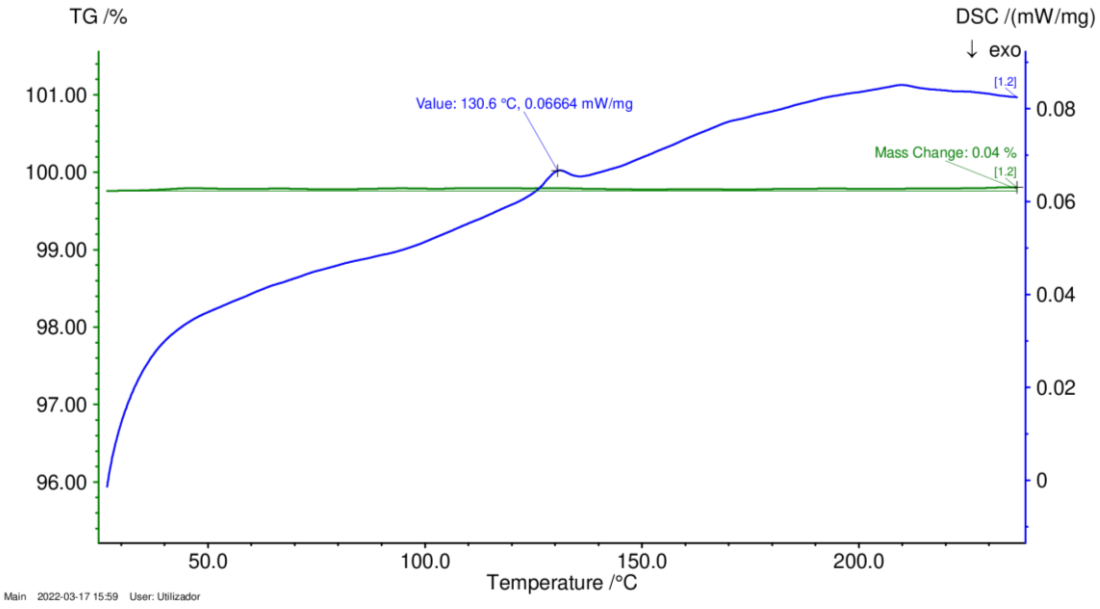

Figure 5. DSC/TG for sample $BaTiO_3$-280nm from 25 ℃ to 220 ℃.

3.2 Hydroxyapatite nanowires

3.2.1 SEM analysis

During the synthesis of HAp NWs, the chemical reactions that take place between the reactants are as follows[39]:

$$C_{18}H_{34}O_2 + NaOH \rightarrow C_{18}H_{33}O_2Na + H_2O \quad 3.2$$

$$2C_{18}H_{33}O_2Na + CaCl_2 \rightarrow (C_{18}H_{33}O_2)_2Ca + 2NaCl \quad 3.3$$

$$NaH_2(PO_4).2(H_2O) + 2OH^- \rightarrow PO_4^{3-} + 4H_2O + Na^+ \quad 3.4$$

$$10(C_{18}H_{33}O_2)_2Ca + 6PO^{3-}_4 + 2OH^- \rightarrow Ca_{10}(PO_4)_6(OH)_2 + 20C_{18}H_{33}O_2 \quad 3.5$$

It can be noticed that the calcium oleate acts as both the calcium source and the precursor for the formation of HAp NWs, while NaH_2PO_4 acts as the phosphorus source. In the beginning of the reaction system, calcium oleate is formed in chemical reactions 3.2 and 3.3. In chemical reaction 3.4, sodium dihydrogen phosphate dihydrate is hydrolyzed to form PO_4^{3-} ions. During the crystallization process in reaction 3.5, Hydroxyapatite nuclei are formed under solvothermal conditions. These nuclei later grow

into longer structures, in a relatively long period of time, under the relatively high temperatures and pressures, as explained in section 2.1.1.

The existence of nanowires was first described by observing, on SEM, the resulting HAp slurry, previously dried on a petri plate at 40 ℃.

In the first place, for synthesis temperatures of 120 ℃, the resulting images present in B IV, Figure B 3, showed no presence of structures for any of the synthesis times: 18, 24 and 30 hours. It should also be noted that the wrinkles present in the samples are attributed to the extraction of the dried HAp sample to a new substract, used in the SEM analysis, thus, being irrelevant for the morphology analysis. It could be speculated that the temperature is too low for the occurrence of the solvothermal reaction, therefore, this temperature for the solvothermal synthesis was automatically rejected for the formation of HAp NWs.

Higher temperatures, such as 165 ℃ and 180 ℃, were evaluated with synthesis times of 5, 7, 18 and 24 hours, with resulting samples presented in Figure 6.

For shorter synthesis times, such as 5 hours, exhibited in a) and c) for 165 ℃ and 180 ℃, respectively, several structures appear to be starting to form. At 165 ℃ some small wires seem to start to form within an undifferentiated structure and at 180 ℃ there seems to be longer wires next to some small rectangular structures, however, they are almost completely blend to each other. Only in d), at 7 hours, some longer structures appear in the vicinity of more differentiated rodlike structures, with around 6μm length. Nevertheless, these longer structures also seem to be merged, preventing them to be differentiated from each other.

In the case of longer synthesis times, the sample f), of 24 hours and 180 ℃, showcases mostly rod structures with around 10μm length, whereas for 18 hours, both samples, b) and e), of 165 ℃ and 180℃ display rodlike structures surrounded by wires. However, it should be noted that, with temperatures of 165 ℃, the wires appear to be somewhat merged similarly to the sample of 7 hours and 180 ℃, present in d).

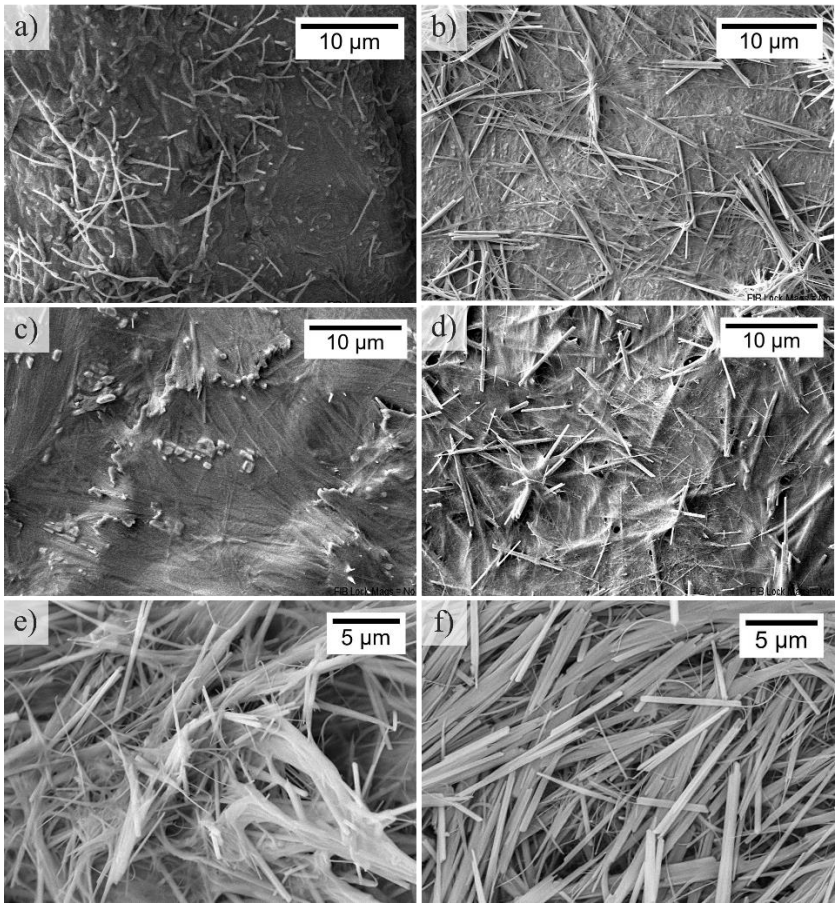

Figure 6. SEM imaging of Hydroxyapatite synthesized at a) 165 °C for 5 h, b) 165 °C for 18 h, c) 180 °C for 5 h, d) 180 °C for 7 h, e) 180 °C for 18 h, f) 180 °C for 24 h.

Accordingly, the most interesting sample was the one of 180 ℃/18 h, which seems to present a higher quantity of wirelike structures, when compared to the other samples. This more intertwined structure of the HAp wires, additionally exhibited in Annex B IV, Figure B 4, could be an advantage in the mechanic abilities of the aerogels.

3.2.2 XRD diffraction analysis

Following the evaluation of the NWs morphology, some of the solvothermal synthesis temperatures were discarded. Therefore, an evaluation of the crystallinity of HAp and existence of other compounds was conducted on the following samples: 165 ℃: 5 and 18 hours and 180 ℃: 5, 7, 18, and 24 hours. In regard to the data treatment of the obtained XRD diffraction spectrum, a created baseline was subtracted to the diffraction data, allowing to better understand the intensity of the peaks relative to each other, in spectrums such as the ones seen in Figure 8.

To evaluate the existence of hydroxyapatite and other impurity compounds, the diffraction peaks were compared to the ICDD sheet of $Ca_{10}(PO_4)_6(OH)_2$, and JCPDS cards of used reagents during the synthesis, such as $CaCl_2$, $NaH_2PO_4.2H_2O$ and NaOH.

Firstly, for either temperature, a synthesis time of 5 h does not lead to the formation of crystalline hydroxyapatite as there is still the presence of wide peaks, more noticeable in Figure 7 a), typical of an

amorphous structure. However, both XRD spectrum of Figure 7 exhibit some characteristic crystalline HAp peaks such as those around 31.7° and 45.4° that can indicate the start of HAp synthesis. It could be noted that, for the same synthesis time, more HAp characteristic peaks were formed at a higher temperature of 180 ℃, present in Figure 7 b), than at 165 ℃, in Figure 7 a). Essentially showing that higher temperatures accelerate the formation of hydroxyapatite crystallites.

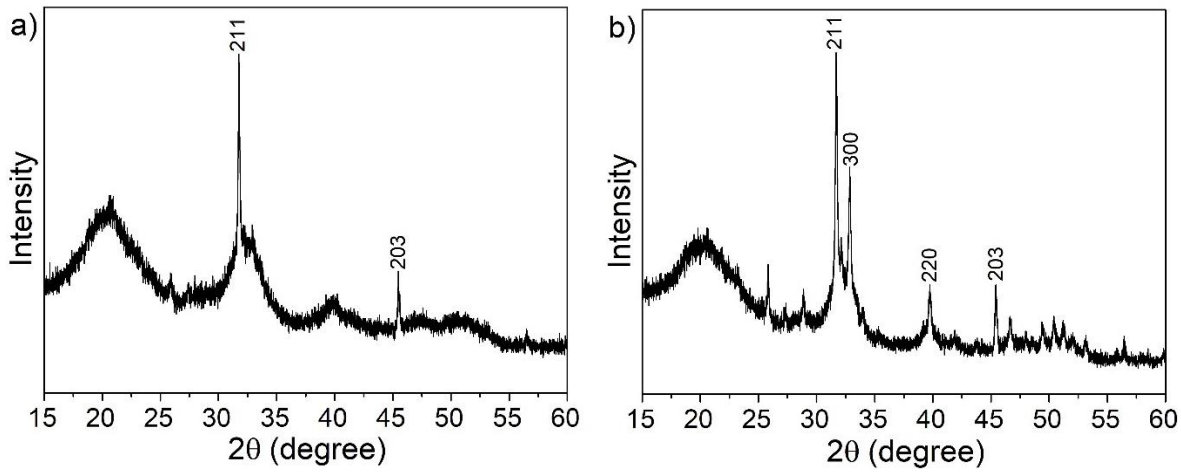

Figure 7. XRD diffraction spectrum for HAp NWs synthesized at a) 165 ºC and b) 180 ºC for 5 h.

The remaining diffraction results, present on Figure 8, clearly show the presence of crystalline hydroxyapatite in all the samples, with all peaks corresponding to the ICDD sheet, although some differences between the relative intensities of the identified peaks can be found. For instance, in the case of the sample of 180 ℃:24 h, the two highest intensities, (211) and (300), are switched when compared to reference data or other samples in Figure 8. This phenomenon could be explained by a preferential formation of crystalline grains along the longitudinal direction of the nanowires, which appear to be the direction perpendicular to the (300) plane, increasing the intensity of the measured peak at 32.8° and highlighting that change, in peak intensities, for the larger structures formed in a synthesis time of 24 hours. In addition, no characteristic peaks of the reagents were found in the diffraction spectra shown in Figure 8.

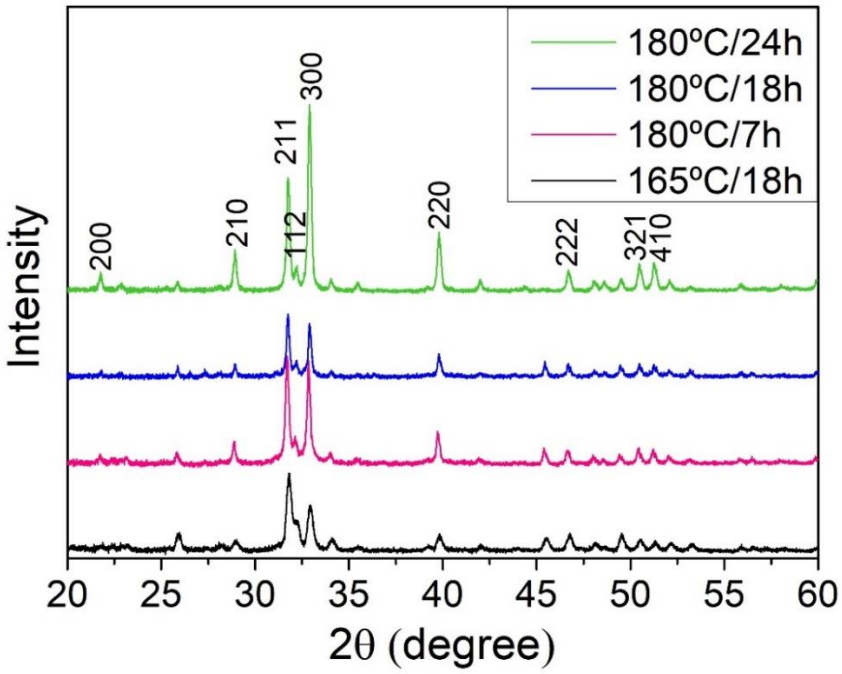

Figure 8. XRD diffraction spectrum for HAp NWs synthesised at diferent temperatures and times.

The chosen synthesis time and temperature for the HAp NWs, which will be used for the fabrication of the HAp aerogels, were 180 ºC and 18 hours due to both the sample's XRD spectra and morphology, as seen in section 3.2.1.

The average size of the crystalline grains, τ, present in the HAp 180 ºC:18 hours sample was calculated to be 39.05 nm, according to equation 3.1, where $2\theta = 31{,}74°$, with a β of 3.694×10^{-3} radians, a $\lambda(Cuk\alpha)$ =1.5418 $\times 10^{-10}$ m and a κ of 0.9[33].

3.2.3 FTIR analysis

In Figure 9, a FTIR analysis of hydroxyapatite synthesized at 180 ℃ for 18 h is shown. The presented spectrum shows a typical HA spectrum containing sharp O–H and P–O bands. The bands of significant intensity, around 1026 cm^{-1} and 1100 cm^{-1}, and the bands near 560 cm^{-1}, 600 cm^{-1} and 960 cm^{-1} correspond to symmetric stretching vibration of the PO_4^{3-} tetrahedral. Moreover, the band around 633 cm^{-1} is attributed to the stretching modes of hydroxyl groups in the hydroxyapatite[40][41][42].

The small band at 870 cm^{-1} indicates the presence of HPO_4^{2-} ions. This observation suggests the existence of non-stoichiometric HAp and the presence of carbonated apatite, which can be confirmed by the characteristic bands between wavenumbers of 1460 cm^{-1} and 1530 cm^{-1}. As seen in Figure 10, two types of substitutions occurred, A-type carbonate substitutions, where carbon ions substitute hydroxyl groups of the hydroxyapatite matrix and B-type carbonate substitutions, resulting from carbonate ions that have substituted phosphate ions[43][44]. It can be concluded that the resulting product from the solvothermal synthesis at 180 ℃ for 18 h is AB-type carbonated apatite. The B-type carbonate substitutions in the apatite lattice are known to increase the extent of solubility in weak acids, a characteristic that can help the substitution of the aerogel with the new bone, when using this material in bone regeneration[45].

Signs of adsorbed water can also be seen on the wide bands that appear on the spectra from 2600 cm^{-1} to around 3600 cm^{-1} and at 1640 cm^{-1}[40].

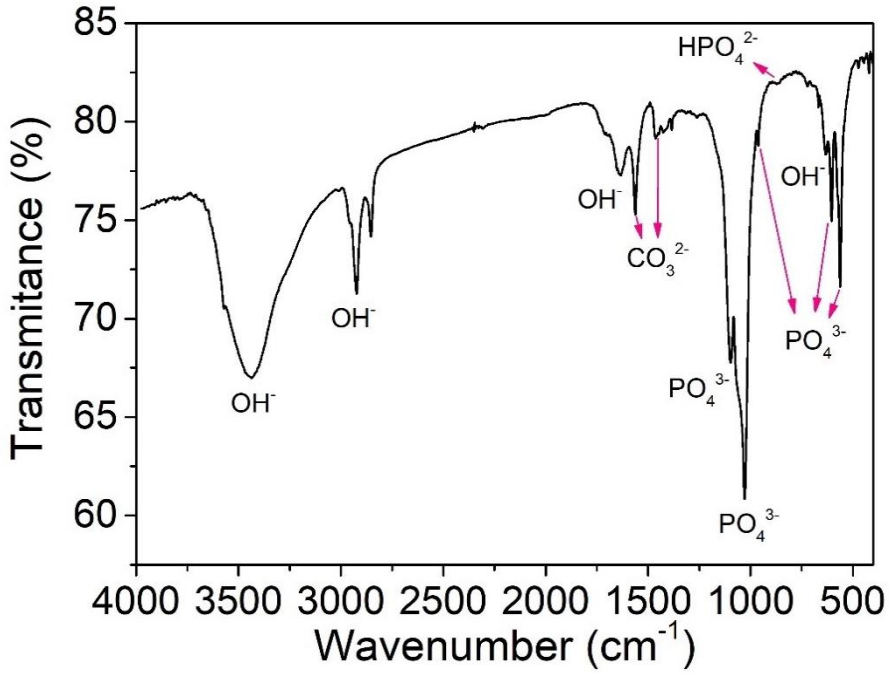

Figure 9. FTIR spectrum of HAp synthesised at 180 ℃ for 18 h.

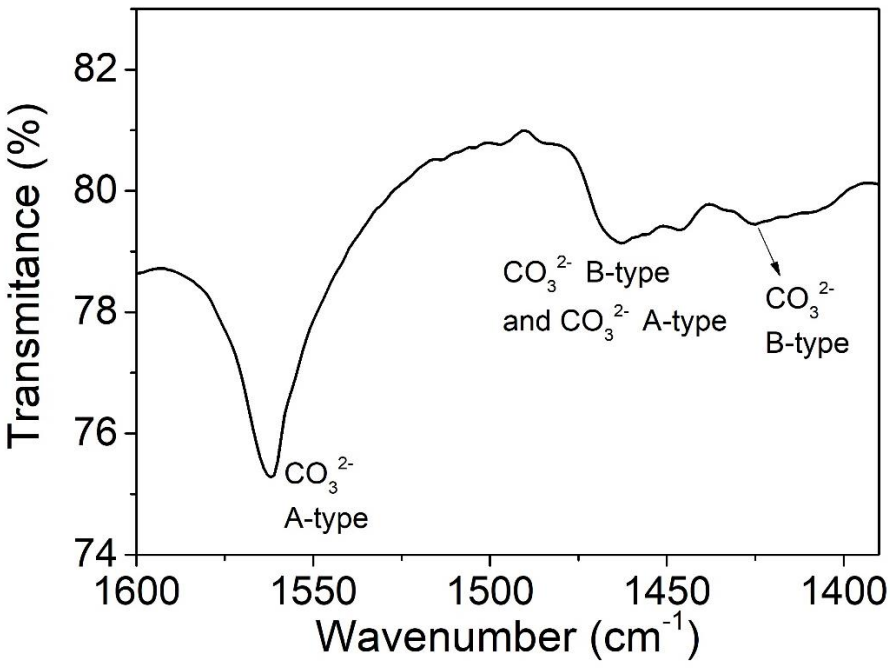

Figure 10. FTIR spectrum, for wavenumbers between 1600 cm^{-1} and 1350 cm^{-1}, of HAp synthesized at 180 ℃ for 18 h.

3.3 Hydroxyapatite/Barium Titanate aerogels

The produced aerogel samples consisted of one sample of HAp aerogel without BaTiO3 particles, denominated HAp, and three HAp aerogels with a 20BT/80HAp (w/w%), named HAp/BT280 for an HAp aerogel embedded with 280 nm sized particles, HAp/BT2 in the case of 2 µm and HAp/BT3 for the aerogel with the 3 µm particles.

3.3.1 Porosity of the aerogels

The porosity of the aerogels was calculated through equation 3.6, as seen in Annex V, where EW is the expected weight of an HAp solid material with the aerogel's dimensions and RW represents its real weight[46]. The samples produced presented an average porosity of 99,68%, for both HAp and HAp/BT aerogels.

$$P(\%) = \frac{RW}{EW} \times 100 \qquad 3.6$$

3.3.2 SEM analysis

The microscopic homogeneity of the HAp and HAp/BT aerogels was investigated by imaging on SEM the surface of the aerogel. The cross sections of the aerogels were not observed due to the fact that the pressure of knife used for cutting the sample would change the porosity of the aerogel by crushing it. Freeze-dried with N2 liquid was tried but not successful.

As it can be seen in Figure 11, all the samples show similar heterogenous porosity throughout, where some regions, with higher connecting NWs surface area, present smaller pores while other areas, due to less interconnectivity between wires, result in the formation of larger pores. The length of the wires was not possible to measure since it varied and the start and end of the wire was not found, however, shorter wires of some shorter wires with a length of approximately 10 µm were found. The diameter of the wires varied, however, it seemed to be less than 1 µm.

Regarding the aerogels HAp/BT280, HAp/BT2 and HAp/BT3, shown in the same Figure 11, the particles seemed to be dispersed evenly throughout the aerogel, however, there seemed to be some agglomerates in certain zones. Increasing the sonication time might help reduce this aggregation between particles and spread them more efficiently.

The aerogels showed to be relatively fragile to handle, since their mechanical stability was most likely affected by its high porosity and the relatively short length of the NWs.

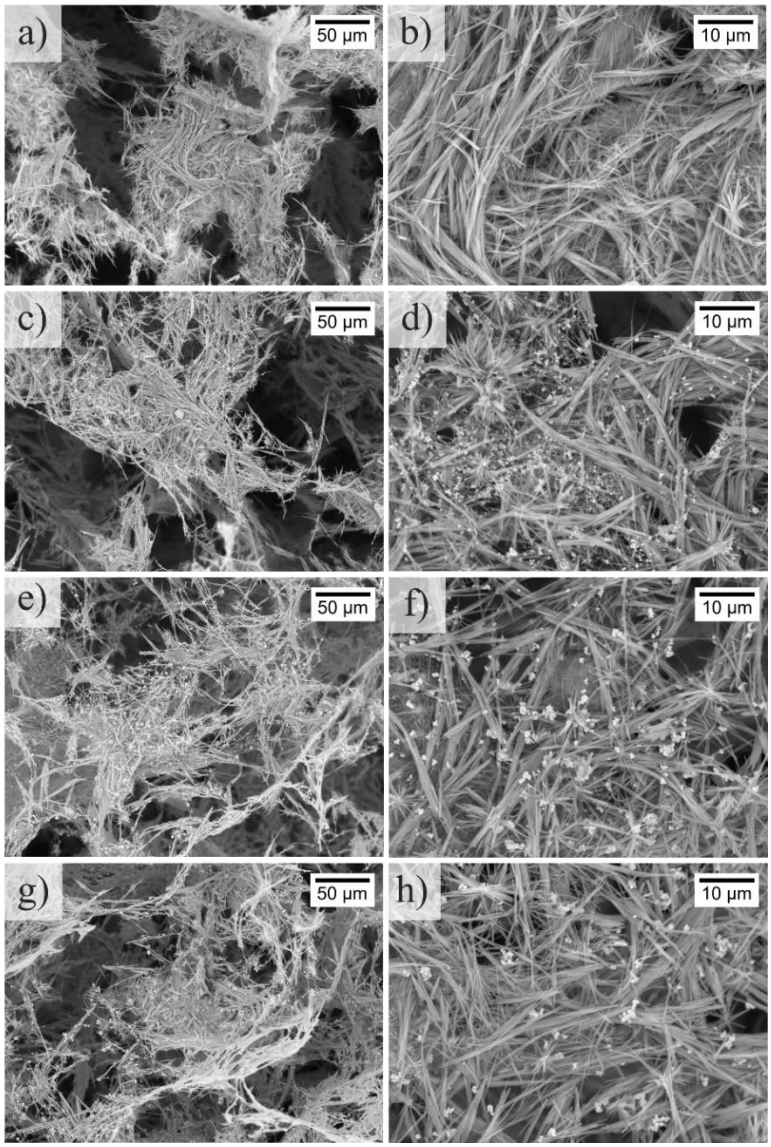

Figure 11. SEM imaging of aerogel samples: a) and b) HAp, c) and d) HAp/BT280, e) and f) HAp/BT2, g) and h) HAp/BT3.

3.3.3 Cytotoxicity tests

In vitro colorimetric assays using resazurin, in conformity with the standard ISO-10993-5 test protocol, explained in annex A I, allowed a study of the potential cytotoxic effect of different dilutions of $BaTiO_3$ particles, sizes, 2µm, 3µm, 280nm, and of the HAp, HAp/BT280, HAp/BT2 and HAp/BT3 aerogels.
The sample distribution along the plate is represented in Annex B VI, Figure B 5 and Figure B 6, with 4 replicas, for each sample, concentration used and respective control mediums. Given the low mass of the aerogels, the chosen concentrations analysed were significantly lower, 1 mg/ml, than the ones used for the $BaTiO_3$ particles, 60 mg/ml.
The relative cell population and its relative uncertainty obtained for each $BaTiO_3$ particle size, corresponding to the highest concentration analysed, is displayed on Figure 12, with all the remaining data is presented in Annex VI, Table B 2.
As seen on the graph of Figure 12, all the $BaTiO_3$ samples revealed high cell viability, with relative cell population above 100%, which can be the result of not only cell survival but also cell proliferation.

Therefore, it is secure to assume that the $BaTiO_3$ samples are non-cytotoxic for all the concentrations studied.

In the case of the fabricated aerogels, the relative cell population, and its relative uncertainty, for different concentrations of the extracts is shown in Figure 13. The same pattern was attested in every sample, where the HAp and HAp/BT3 samples were considered severely cytotoxic while the HAp/BT280 and HAp/BT2 samples were moderately cytotoxic for the highest concentration used. For the following dilutions all samples showed a non-cytotoxic response.

However, a relative cell population of 140% is unusually high to be justified purely by cell viability and proliferation. It could be speculated that the reduction of resazurin is being affected by other parameters, and that the results obtained might not be reliable.

According to Klimek, et. al.[47], the apparent cytotoxicity of the hydroxyapatite might be caused by a massive uptake of with Ca^{2+} and HPO_4^{2-} ions from the medium, related to the high surface area of the ceramics, resulting in extracts not optimal for cell cultures. This phenomenon will lead to an unexpected cytotoxic effect despite these ion reactions being correlated with increased bioactivity. Moreover, in vivo, tissue liquids continuously circulate around implanted biomaterial and supplement all the adsorbed ions in the implantation area. This could be the case of the fabricated ceramics since Gustavsson et al.[48] also reported ion adsorption by calcium-deficient hydroxyapatite with a carbonated surface chemistry, similar to the AB–type carbonated apatite's chemistry observed in FTIR in the section 3.2.3. At lower concentrations of the extracts, the uptake of ions might not be enough to lead to cell death, however, it can still influence the natural behavior of the viable cells, leading them to release enzymes that reduce resazurin, obtaining an over estimation of the cell population[49].

To conclude if the material is indeed cytotoxic, it is suggested a modified method for the evaluation of cytotoxicity, more appropriate for ions-adsorbing ceramics than the ISO 10993-5 standard. That is, to first measure the concentration of Ca^{2+} and HPO_4^{2-} ions in the obtained ceramic´s extract. If the extract's concentration of Ca^{2+} and HPO_4^{2-} ions is significantly lower than the control medium extract, suggesting that the biomaterial absorbs ions, the extract can be supplemented with Ca^{2+} and HPO_4^{2-} to reach the level similar to that of culture control medium, before the cell viability is tested. If the ion concentrations are close to those in control medium, then biomaterial is releasing toxic substance and exhibits "true" cytotoxicity[47].

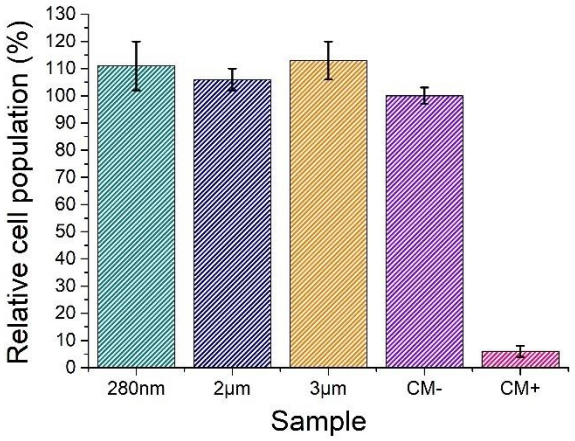

Figure 12. Histogram data from the cytotoxicity tests of $BaTiO_3$ particles, 280 nm, 2 µm, 3 µm, negative (CM-) and positive (CM+) control groups for a dilution factor of 60mg/ml.

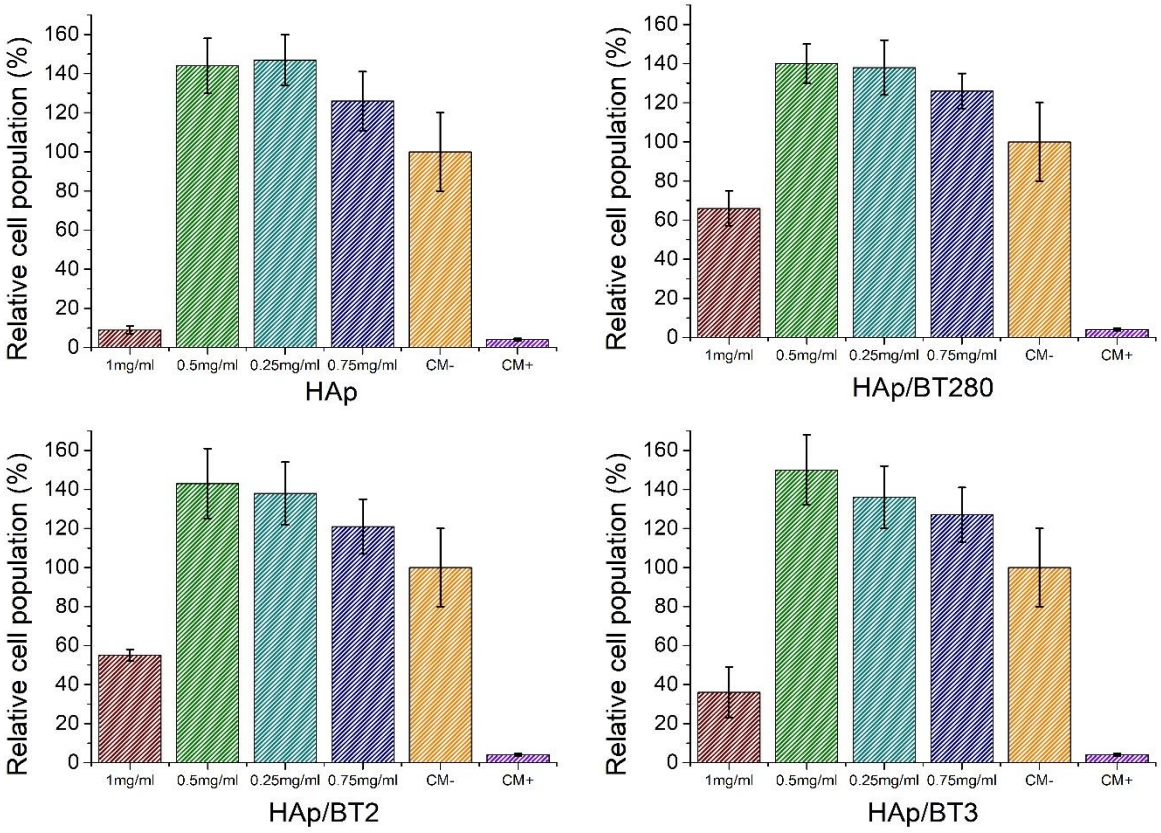

Figure 13. Histogram data from the cytotoxicity tests of the fabricated aerogels, HAp, HAp/BT280, HAp/BT2, HAp/BT3 and negative (CM-) and positive (CM+) control groups.

3.3.4 Bioactivity assays in simulated body fluid

The bioactivity was analyzed by submerging the aerogels HAp, HAp/BT280, HAp/BT2, HAp/BT3 in an SBF solution and left at 37 ºC, mimicking average body temperature, for 1 day, 3 days, and 7 days, and by preparing a control group which was not submerged. The immersed aerogels did not hold their shape, and collapsed, ending up behaving as HAp NWs. Given the new surface area that is in contact with the SBF, the new minimum quantity of SBF that should be used was calculated according to Maçon et. al[50], to be 75 mg to 50 mL of SBF, which aligned with the value calculated in section 2.2.5. Therefore, no changes were made.

All samples were analyzed through SEM images and EDS data.

The EDS analysis confirmed the FTIR results, in section 3.2.3, about the presence of carbon in the samples as seen in Figure B 10- B 13.

In Figure 14, for the SEM images of the HAp aerogel, there was no clear deposition of apatite structures in any immersion time evaluated. The same occurred for the remaining samples in Annex BVII, Figure B 7, Figure B 8 Figure B 9.

It is noticeable that there is still some residue of Na and Cl, especially in the samples of 7 days, as shown in the EDS analysis, Annex B VII, Figure B 26 to Figure B 33, which hinders, in some areas, the observation of a clearer image of the wires. This fact difficulted the comparison of the sample's SEM images and EDS maps with the control groups and prevented from concluding if the low definition of the wires originated from deposition of CaP followed by dissolution or from NaCl structures. The rough morphology and chemistry of the sample, which naturally contains CaP, could also be preventing the observation of deposited CaP in the case of relatively small crystals.

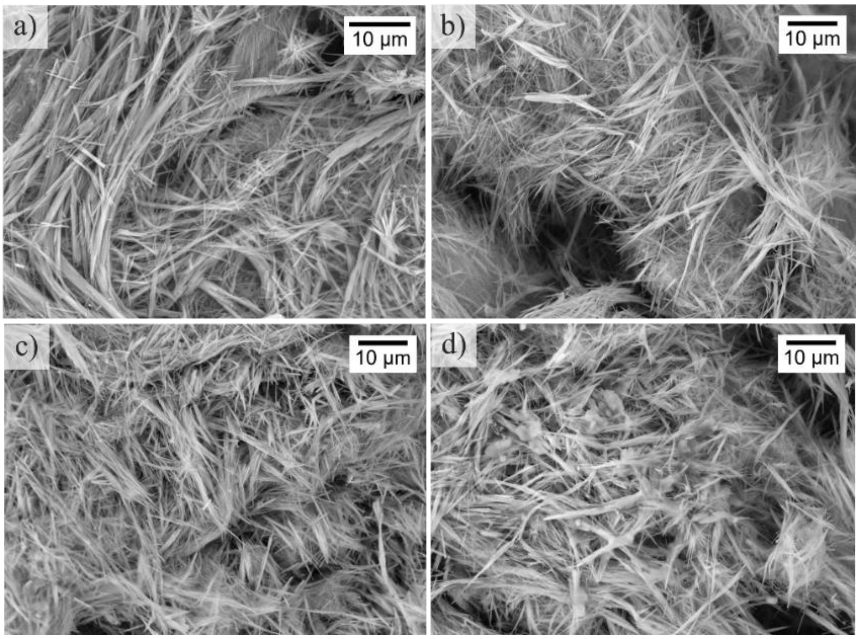

Figure 14. SEM images of HAp aerogel a) with no days in SBF, b) after 1 day in SBF, c) after 3 days in SBF, d) after 7 days in SBF.

Since the SEM imaging and EDS mapping does not confirm if CaP deposition occurred, quantity EDS analysis, present in Annex BVII was used, and the Calcium/Phosphate ratio (Ca/P) for all the samples were calculated. In this way deposition/dissolution process of an apatite layer can be evaluated.

In Figure 15, the evolution of the ratios with the immersion time is similar between samples, with an increase on the first three days and a decrease on the seventh. It could be possible that some cycle of Ca/P deposition followed by dissolution is occurring in a scale that is not visible in the obtained SEM images. Since the produced hydroxyapatite seems to be calcium deficient, due to a Ca/P ratio of 1.5 before SBF immersion, the described cycle might be promoted by an initial deposition of calcium, increasing the Ca/P ratio.

At the SEM magnification that was allowed by the equipment, either the crystals formed are very small or there was a thin continuous layer of deposited CaP that could not be distinguished from the original NWs surface.

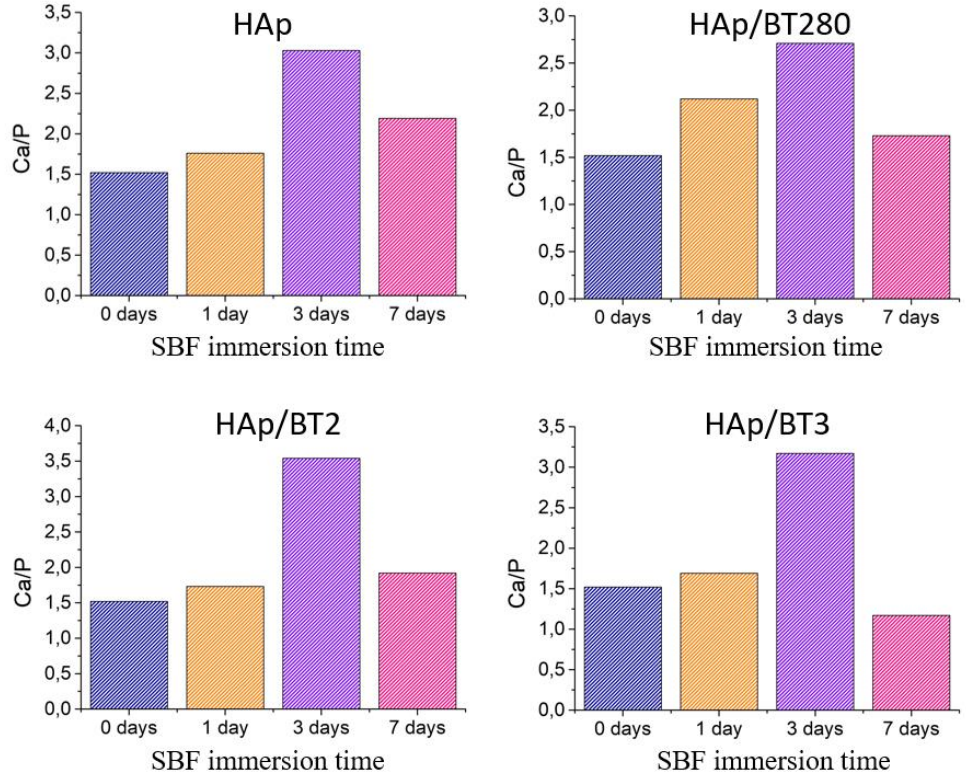

Figure 15. Ca/P ratios of the Hap and Hap/BT aerogels, calculated by a quantifying EDS analysis, after SBF immersion.

Regarding the calcium phosphate deposition on the $BaTiO_3$ particles, from the SEM imaging data present in Annex B VII, Figure B 7,Figure B 8 Figure B 9, it is possible to note that, after 7 days, no apparent apatite deposition occurred in the barium titanate particles present in the aerogel.

4

CONCLUSION

The main goal of this dissertation was the production of HAp aerogels and HAp and $BaTiO_3$ composite aerogels and to study its potential use in biomedical applications for bone regeneration.

Firstly, the commercially bought $BaTiO_3$ particles were characterized by XRD, FTIR, Raman. By the XRD diffractogram, it was possible to verify that the chemical composition of the powders was in accordance with the suppliers and tetragonal phase of barium titanate was detected in all samples. The tetragonal phase was mainly perceived by the existence of a peak split around $2\theta=45°$, which was more visible on the 280nm powders, as expected for small grain size, peaks were more sharp and well defined. The chemical groups of $BaTiO_3$ where further confirmed by FTIR, where the spectrum presented the existence of Ti-O bonds attributed to $BaTiO_3$. Possibly due to compounds with carbon, used in the synthesis of $BaTiO_3$, such as barium carbonate, a C-O bond was also detected in the samples.

Raman results showed active modes typical of tetragonal $BaTiO_3$, confirming the presence of a tetragonal phase in accordance with the XRD results.

A thermal analysis, DSC/TG, was made, but unfortunately, it was only possible to observe an endothermic peak on the sample of 280 nm. Since the expected shift should occur around $BaTiO_3$ Curie temperature, and the chemical analysis confirmed the existence of $BaTiO_3$, it is proposed that the absence of peaks on the 2 µm and 3 µm sample took place due to being less sharp and well defined. To be able to observe this transition on the micrometric BT powders, a higher resolution of the measuring equipment on the temperature range close to Curie temperature is needed.

Considering the main objective, this work continued with the synthesis and characterization of HAp NWs to be used in the fabrication of the aerogels. The product of the solvothermal reaction was observed over SEM, proving the formation of several structures over different reaction times and temperatures. For a temperature of 180 °C, only over 7 h of synthesis, clear differentiated structures started to form. At 18 h it was possible to observe more wire like structures intertwined with rods and at 24 h the product manly resulted in rodlike structures. A solvothermal synthesis at temperatures of 165 °C, also resulted on differentiated wire structures for a time of 18 h.

The selected samples, 165 °C:18 h and 180 °C: 7, 18, and 24 h, were chemically identified to be hydroxyapatite by XRD analysis while the samples of 5 h did not allow the completion of the HAp synthesis. Finally, the sample of 180 °C:18h was chosen for the synthesis of aerogels due to the existence of well-defined and longer wires observed in SEM and its XRD spectrum typical of hexagonal HAp.

According to the FTIR measurements realized on the chosen sample, the spectrum presented chemical groups typical of HAp, such as O–H and P–O bands, and a number of carbonate substituents, leading to the conclusion that the synthesis resulted in AB-type carbonated hydroxyapatite. This could be an improved feature regarding bone regeneration.

Following this, the formation of the HAp aerogel structures and the integration of 20% (w/w) of $BaTiO_3$ particles into the aerogels was studied. The aerogels showed an average porosity of 99.68% for both the HAp and HAp/BT and, under SEM, their morphology seemed homogeneous throughout, with interlinked wires and heterogenous pore sizes. The measurements of the wires varied and were difficult to measure due to their intertwined positions, however, it was possible to see some wires with a length of approximately 10 µm, while their diameters appear to be from a maximum of 1 µm to some hundredths of nm.

It is important to notice that the aerogels were fragile to handle, possibly due to both its high porosity and the relative short size of the HAp wires.

Regarding the dispersion of $BaTiO_3$ particles on the HAp/BT280, HAp/BT2 and HAp/BT3 aerogels, their distribution seemed homogenous despite some small aggregates. Increasing the sonication time when mixing the particles and the HAp NWs slurry might help to efficiently spread the particles avoiding the use of a surfactant.

Cytotoxicity assays, based on the the standard ISO-10993-5 test protocol, considered that all the $BaTiO_3$ particles were non-cytotoxic for a concentration of 50 mg/ml, while, a concentration of 1 mg/ml, for all the aerogels, HAp, HAp/BT280, HAp/BT2 and HAp/BT3, showed a cytotoxic response. There are two possible outcomes form these results, either the aerogels are releasing some toxic substance or, since the aerogels presented to be carbonated hydroxyapatite, there might be occurring massive absorption of Ca^{2+} and HPO_4^{2-} ions from the medium during the cytotoxicity assays, which is not ideal for cell cultures. This leads to a cytotoxic response although the material is not truly cytotoxic in *in vivo* implantation, for the concentration studied.

Difficulties were found, in the bioactivity assays, when trying to differentiate between the possibly deposited apatite structures and the surface of the HAp wires. Despite the obtained SEM images and EDS mapping data not showing clear apatite structures, the evolution of the sample's Ca/P ratios with the SBF immersion time, calculated by quantitative EDS analysis, shows that there is a possibly a cycle of CaP deposition followed by dissolution occurring. Significative differences between the samples were not found.

Regarding the continuation of the work, the study completed in this dissertation can enable future research on the bone regenerative properties of the fabricated aerogel structures. For instance, future studies could focus on improving the mechanical stability of the aerogels. It is proposed to not only study new temperatures and times for the solvothermal reaction in order to increase the size of the wirelike structures but also increase the quantity of wires in the slurry that was later freeze dried in the culture cell plate wells. While that could slightly reduce the porosity of the aerogel, they might prove to be less fragile due to higher interconnectivity of the NWs.

However, additional cytotoxic assays that account for the HAp's adsorption of ions from the medium, and better mimic the body´s ability to supplement adsorbed ions, could be performed to confirm the cytotoxicity of the synthesized material and decide the viability of the fabricated aerogels for the intended applications.

The bioactivity tests should also be repeated, with better washing of the samples to remove NaCl and to improve the clarity of the structures on the SEM images and EDS analysis. This could be easier obtained with more stable aerogel when immersed in SBF. To better understand and quantify the deposition of apatites in the HAp NWs, inductively coupled plasma mass spectrometry (ICP-MS) could be used to detect shifts in the concentration of Ca^{+} and P^{3-} on the SBF medium. If there is truly a deposition of apatites, detected more clearly by SEM/EDS and ICP-MS, a larger time frame for the bioactivity tests could also allow for better observation of SEM images of apatite deposition on the samples.

Potential tests for the cell adhesion and proliferation of the aerogels, once they show to be less fragile, could prove interesting to better characterize the material for bone regeneration applications.

The presence of tetragonal $BaTiO_3$ on HAp aerogels, which was studied in this dissertation, and its respective piezoelectric capabilities, might allow conducting future studies on the influence of electric charges on the bioactivity, cell proliferation and adhesion of the aerogels. There are some contradictions found between several experiments regarding polarized samples, especially regarding cell activity on positively charged surfaces, possibly due to factors such as the material, surface roughness and topology of the ceramics used in the experiments, which may differ, or the fact that methods of test vary in terms of the cell types tested and other procedural aspects. In particular, in vitro testing, cell culture studies do not consider the presence of blood at the implant site. So, the existence of more studies could prove beneficial to increase the available data and better address the conflicting results found in literature.

BIBLIOGRAPHY

[1] Y. Wei and Y. Sun, "Aging of the bone," *Adv. Exp. Med. Biol.*, vol. 1086, pp. 189–197, 2018, doi: 10.1007/978-981-13-1117-8_12.

[2] F. G. F. Tresguerres, J. Torres, J. López-Quiles, G. Hernández, J. A. Vega, and I. F. Tresguerres, "The osteocyte: A multifunctional cell within the bone," *Ann. Anat.*, vol. 227, p. 151422, 2020, doi: 10.1016/j.aanat.2019.151422.

[3] S. V. Dorozhkin, "Current state of bioceramics," *J. Ceram. Sci. Technol.*, vol. 9, no. 4, pp. 353–370, 2018, doi: 10.4416/JCST2018-00026.

[4] D. F. Williams, "On the nature of biomaterials," *Biomaterials*, vol. 30, no. 30, pp. 5897–5909, 2009, doi: 10.1016/j.biomaterials.2009.07.027.

[5] G. L. Koons, M. Diba, and A. G. Mikos, "Materials design for bone-tissue engineering," *Nat. Rev. Mater.*, vol. 5, no. 8, pp. 584–603, 2020, doi: 10.1038/s41578-020-0204-2.

[6] S. Oh, N. Oh, M. Appleford, and J. L. Ong, "Bioceramics for Tissue Engineering Applications: A Review," *Am. J. Biochem. Biotechnol.*, vol. 2, no. 2, pp. 49–56, 2006, doi: 10.3844/ajbbsp.2006.49.56.

[7] H. Qu, H. Fu, Z. Han, and Y. Sun, "Biomaterials for bone tissue engineering scaffolds: A review," *RSC Adv.*, vol. 9, no. 45, pp. 26252–26262, 2019, doi: 10.1039/c9ra05214c.

[8] M. P. Nikolova and M. S. Chavali, "Recent advances in biomaterials for 3D scaffolds: A review," *Bioact. Mater.*, vol. 4, no. October 2019, pp. 271–292, 2019, doi: 10.1016/j.bioactmat.2019.10.005.

[9] R. K. Fuchs, W. R. Thompson, and S. J. Warden, *Bone biology*, Second Edi. Elsevier Ltd, 2019.

[10] R. Florencio-Silva, G. R. D. S. Sasso, E. Sasso-Cerri, M. J. Simões, and P. S. Cerri, "Biology of Bone Tissue: Structure, Function, and Factors That Influence Bone Cells," *Biomed Res. Int.*, vol. 2015, 2015, doi: 10.1155/2015/421746.

[11] B. Clarke, "Normal bone anatomy and physiology.," *Clin. J. Am. Soc. Nephrol.*, vol. 3 Suppl 3, pp. 131–139, 2008, doi: 10.2215/CJN.04151206.

[12] N. M. Iñiguez-Ariza and B. L. Clarke, "Bone biology, signaling pathways, and therapeutic targets for osteoporosis," *Maturitas*, vol. 82, no. 2, pp. 245–255, 2015, doi: 10.1016/j.maturitas.2015.07.003.

[13] N. Eliaz and N. Metoki, "Calcium phosphate bioceramics: A review of their history, structure, properties, coating technologies and biomedical applications," *Materials (Basel).*, vol. 10, no. 4, 2017, doi: 10.3390/ma10040334.

[14] D. S. Gomes, A. M. C. Santos, G. A. Neves, and R. R. Menezes, "A brief review on hydroxyapatite production and use in biomedicine," *Ceramica*, vol. 65, no. 374, pp. 282–302, 2019, doi: 10.1590/0366-69132019653742706.

[15] S. Samavedi, A. R. Whittington, and A. S. Goldstein, "Calcium phosphate ceramics in bone tissue engineering: a review of properties and their influence on cell behavior," *Acta Biomater.*, vol. 9, no. 9, pp. 8037–8045, 2013, doi: 10.1016/J.ACTBIO.2013.06.014.

[16] I. Sopyan, M. Mel, S. Ramesh, and K. A. Khalid, "Porous hydroxyapatite for artificial bone

applications," *Sci. Technol. Adv. Mater.*, vol. 8, no. 1–2, pp. 116–123, 2007, doi: 10.1016/j.stam.2006.11.017.
[17] N. Abbasi, S. Hamlet, R. M. Love, and N. T. Nguyen, "Porous scaffolds for bone regeneration," *J. Sci. Adv. Mater. Devices*, vol. 5, no. 1, pp. 1–9, Mar. 2020, doi: 10.1016/J.JSAMD.2020.01.007.
[18] G. J. Huang *et al.*, "Highly porous and elastic aerogel based on ultralong hydroxyapatite nanowires for high-performance bone regeneration and neovascularization," *J. Mater. Chem. B*, vol. 9, no. 5, pp. 1277–1287, 2021, doi: 10.1039/d0tb02288h.
[19] Z. C. Xiong, Z. Y. Yang, Y. J. Zhu, F. F. Chen, Y. G. Zhang, and R. L. Yang, "Ultralong Hydroxyapatite Nanowires-Based Paper Co-Loaded with Silver Nanoparticles and Antibiotic for Long-Term Antibacterial Benefit," *ACS Appl. Mater. Interfaces*, vol. 9, no. 27, pp. 22212–22222, 2017, doi: 10.1021/acsami.7b05208.
[20] F. R. Baxter, C. R. Bowen, I. G. Turner, and A. C. E. Dent, "Electrically active bioceramics: A review of interfacial responses," *Ann. Biomed. Eng.*, vol. 38, no. 6, pp. 2079–2092, 2010, doi: 10.1007/s10439-010-9977-6.
[21] E. Fukada and I. Yasuda, "piezoeletric effect to the bone.pdf." J. Phys. Soc. Jpn., Kobayasi Institute of physical Research, Kokulunji, Tokyo, 1957.
[22] G. Yao *et al.*, "A self-powered implantable and bioresorbable electrostimulation device for biofeedback bone fracture healing," *Proc. Natl. Acad. Sci. U. S. A.*, vol. 118, no. 28, 2021, doi: 10.1073/pnas.2100772118.
[23] S. Itoh, S. Nakamura, M. Nakamura, K. Shinomiya, and K. Yamashita, "Enhanced bone regeneration by electrical polarization of hydroxyapatite," *Artif. Organs*, vol. 30, no. 11, pp. 863–869, 2006, doi: 10.1111/j.1525-1594.2006.00313.x.
[24] M. Nakamura, A. Nagai, and K. Yamashita, "Surface electric fields of apatite electret promote osteoblastic responses," *Key Eng. Mater.*, vol. 529–530, no. 1, pp. 357–360, 2013, doi: 10.4028/www.scientific.net/KEM.529-530.357.
[25] M. Nakamura *et al.*, "Regulation of osteoblast-like cell behaviors on hydroxyapatite by electrical polarization," *Key Eng. Mater.*, vol. 361-363 II, pp. 1055–1058, 2008, doi: 10.4028/www.scientific.net/kem.361-363.1055.
[26] K. S. Hwang *et al.*, "Effect of poling conditions on growth of calcium phosphate crystal in ferroelectric BaTiO3 ceramics," *J. Mater. Sci. Mater. Med.*, vol. 13, no. 1, pp. 133–138, 2002, doi: 10.1023/A:1013671526975.
[27] J. P. Ball, B. A. Mound, J. C. Nino, and J. B. Allen, "Biocompatible evaluation of barium titanate foamed ceramic structures for orthopedic applications," *J. Biomed. Mater. Res. Part A*, vol. 102, no. 7, pp. 2089–2095, Jul. 2014, doi: 10.1002/JBM.A.34879.
[28] V. Buscaglia and C. A. Randall, "Size and scaling effects in barium titanate. An overview," *J. Eur. Ceram. Soc.*, vol. 40, no. 11, pp. 3744–3758, 2020, doi: 10.1016/j.jeurceramsoc.2020.01.021.
[29] M. Majkut, J. E. Daniels, J. P. Wright, S. Schmidt, J. Oddershede, and J. Ihlefeld, "Electromechanical Response of Polycrystalline Barium Titanate Resolved at the Grain Scale," *J. Am. Ceram. Soc.*, vol. 100, no. 1, pp. 393–402, 2017, doi: 10.1111/jace.14481.
[30] International organization for standardization, "International organization for standardization (2007) Implants for surgery — In vitro evaluation for apatite-forming ability of implant materials standardization," *2007*, vol. 2007, p. 13, 2007.
[31] A. Cüneyt Tas, "Synthesis of biomimetic Ca-hydroxyapatite powders at 37°C in synthetic body fluids," *Biomaterials*, vol. 21, no. 14, pp. 1429–1438, Jul. 2000, doi: 10.1016/S0142-9612(00)00019-3.
[32] H. Qian *et al.*, "Preparation of tetragonal barium titanate nanopowders by microwave solid-state synthesis," *Appl. Phys. A Mater. Sci. Process.*, vol. 126, no. 4, 2020, doi: 10.1007/s00339-020-03472-y.
[33] B. Ingham and M. F. Toney, *X-ray diffraction for characterizing metallic films*. 2013.
[34] H.-W. Lee, S. Moon, C.-H. Choi, and D. K. Kim, "Synthesis and Size Control of Tetragonal Barium Titanate Nanopowders by Facile Solvothermal Method," Journal of the American 33

Ceramic Society Vol. 95, Issue 8, pp. 2429-2434, 2012, doi: 10.1111/j.1551-2916.2012.05085.x.
[35] M. Singh, B. C. Yadav, A. Ranjan, M. Kaur, and S. K. Gupta, "Synthesis and characterization of perovskite barium titanate thin film and its application as LPG sensor," *Sensors Actuators B Chem.*, vol. 241, pp. 1170–1178, Mar. 2017, doi: 10.1016/J.SNB.2016.10.018.
[36] Z. Lazarević *et al.*, "Characterization of barium titanate ceramic powders by Raman spectroscopy," *Acta Phys. Pol. A*, vol. 115, no. 4, pp. 808–810, 2009, doi: 10.12693/APhysPolA.115.808.
[37] V. Sherlin Vinita *et al.*, "Structural, Raman and optical investigations of barium titanate nanoparticles," *Phosphorus, Sulfur Silicon Relat. Elem.*, vol. 197, no. 3, pp. 169–175, 2022, doi: 10.1080/10426507.2021.1993850.
[38] K. I. Sakayori *et al.*, "Curie temperature of $BaTiO_3$," *Jpn. J. Appl. Phys.*, vol. 34, no. 9, pp. 5443–5445, Sep. 1995, doi: 10.1143/JJAP.34.5443/XML.
[39] Y. Y. Jiang, Y. J. Zhu, F. Chen, and J. Wu, "Solvothermal synthesis of submillimeter ultralong hydroxyapatite nanowires using a calcium oleate precursor in a series of monohydroxy alcohols," *Ceram. Int.*, vol. 41, no. 4, pp. 6098–6102, 2015, doi: 10.1016/j.ceramint.2014.12.122.
[40] L. Berzina-Cimdina and N. Borodajenko, "Research of Calcium Phosphates Using Fourier Transform Infrared Spectroscopy," *Infrared Spectrosc. - Mater. Sci. Eng. Technol.*, 2012, doi: 10.5772/36942.
[41] H. Gheisari, E. Karamian, and M. Abdellahi, "A novel hydroxyapatite -Hardystonite nanocomposite ceramic," *Ceram. Int.*, vol. 41, no. 4, pp. 5967–5975, 2015, doi: 10.1016/j.ceramint.2015.01.033.
[42] M. A. El Mhammedi, M. Achak, M. Bakasse, and A. Chtaini, "Physico-chemical characterization of electrochemical deposit of Ca 10 (PO 4) 6 (OH) 2 on copper surfaces," *Appl. Surf. Sci.*, vol. 253, no. 14, pp. 5925–5930, 2007, doi: 10.1016/j.apsusc.2007.01.085.
[43] H. Madupalli, B. Pavan, and M. M. J. Tecklenburg, "Carbonate substitution in the mineral component of bone: Discriminating the structural changes, simultaneously imposed by carbonate in A and B sites of apatite," *J. Solid State Chem.*, vol. 255, no. July, pp. 27–35, 2017, doi: 10.1016/j.jssc.2017.07.025.
[44] F. Ren and Y. Leng, "Carbonated apatite, Type-A or Type-B?," *Key Eng. Mater.*, vol. 493–494, pp. 293–297, 2012, doi: 10.4028/www.scientific.net/KEM.493-494.293.
[45] A. Nagai, K. Tanaka, Y. Tanaka, M. Nakamura, K. Hashimoto, and K. Yamashita, "Electric polarization and mechanism of B-type carbonated apatite ceramics," *J. Biomed. Mater. Res. Part A*, vol. 99A, no. 1, pp. 116–124, Oct. 2011, doi: 10.1002/JBM.A.33131.
[46] H. Sehaqui *et al.*, "High-porosity aerogels of high specific surface area prepared from nanofibrillated cellulose (NFC)" Composites Science and Technology vol. 71, pp. 1593–1599, 2011, doi: 10.1016/j.compscitech.2011.07.003.
[47] K. Klimek *et al.*, "'False' cytotoxicity of ions-adsorbing hydroxyapatite — Corrected method of cytotoxicity evaluation for ceramics of high specific surface area," *Mater. Sci. Eng. C*, vol. 65, pp. 70–79, Aug. 2016, doi: 10.1016/J.MSEC.2016.03.105.
[48] J. Gustavsson, M. P. Ginebra, E. Engel, and J. Planell, "Ion reactivity of calcium-deficient hydroxyapatite in standard cell culture media," *Acta Biomater.*, vol. 7, no. 12, pp. 4242–4252, Dec. 2011, doi: 10.1016/J.ACTBIO.2011.07.016.
[49] J. O'Brien, I. Wilson, T. Orton, and F. Pognan, "Investigation of the Alamar Blue (resazurin) fluorescent dye for the assessment of mammalian cell cytotoxicity," *Eur. J. Biochem.*, vol. 267, no. 17, pp. 5421–5426, 2000, doi: 10.1046/j.1432-1327.2000.01606.x.
[50] A. L. B. Maçon *et al.*, "A unified in vitro evaluation for apatite-forming ability of bioactive glasses and their variants," *J. Mater. Sci. Mater. Med.*, vol. 26, no. 2, pp. 1–10, 2015, doi: 10.1007/s10856-015-5403-9.

A

ANNEX - MATERIALS AND METHODS

I. ISO-10993 "Biological evaluation of medical devices, Part 5: Tests for in vitro cytotoxicity" test protocol

Extracts of the samples were prepared by leaving them in contact with SBF (Phosphate Buffered Saline, 14190 – DPBS, no calcium no magnesium, ThermoFisher, (http://www.thermofisher.com/pt/en/home/technical-resources/media-formulation.147.html) for 24 hours, with different dilution factors such as 1, $\frac{1}{2}$, $\frac{1}{4}$, $\frac{1}{8}$.

Additionally, 8000 Vero cells (DMEM, Sigma-Aldrich) were seeded in each well and after 24h, the culture medium, in which the cells were placed, was extracted and substituted the previously mentioned extracts and control mediums. The control mediums prepared consist of a positive control (cytotoxic), where no cells were added in the well and negative control (non-cytotoxic) where SBF was added to the seeded cells.

In accordance with the standard ISO 10993-5, the cells were left in contact with the extracts and control groups for 48 hours. Following that, the viability of the cells was evaluated by extracting the medium and adding a medium of resazurin (https://www.alfa.com/en/catalog/B21187/) composed by 50% complete culture medium and 50% resazurin solution at 0.04mg/ml in PBS.

II. Protocol for Simulated Body Fluid solution

For 1 liter of SBF, add the following reagents in the presented order to 750 mL of millipore water while stirring at 37 ºC:

- 1.7,996 g of NaCl
- 0,35 g of $NaHCO_3$
- 0,224 g of KCl
- 0,228 g of $Na_2HPO_4.H_2O$
- 0,228 g of $MgCl_2.6H_2O$
- 15 mL of 1M HCl
- 0,0278 g of $CaCl_2.2H_2O$

- 0,0071 g of Na_2SO_4
- 6,057 g of $(CH_2OH)_3CNH_2$.

Measure the pH of the solution and, keeping the electrode submerged, add 1 M HCl drop by drop until the solution reaches a pH value of 7,4. Add millipore water to the solution until it reaches 1 liter. Keep the solution in a refrigerator for up to 1 month, heating it to 37 ºC before using.

B

ANNEX - RESULTS AND DISCUSSION

III. DSC/TG analysis of the $BaTiO_3$ samples

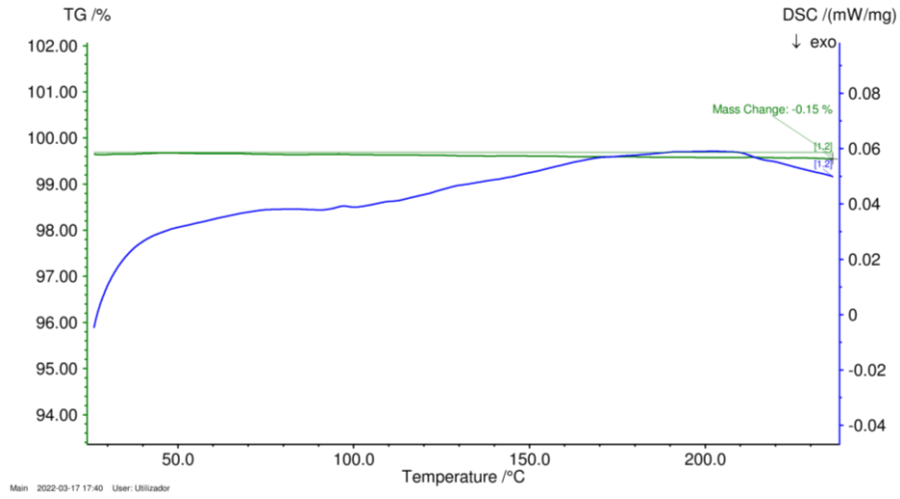

Figure B 1. DSC for sample BT-2µm from 25 ℃ to 220 ℃.

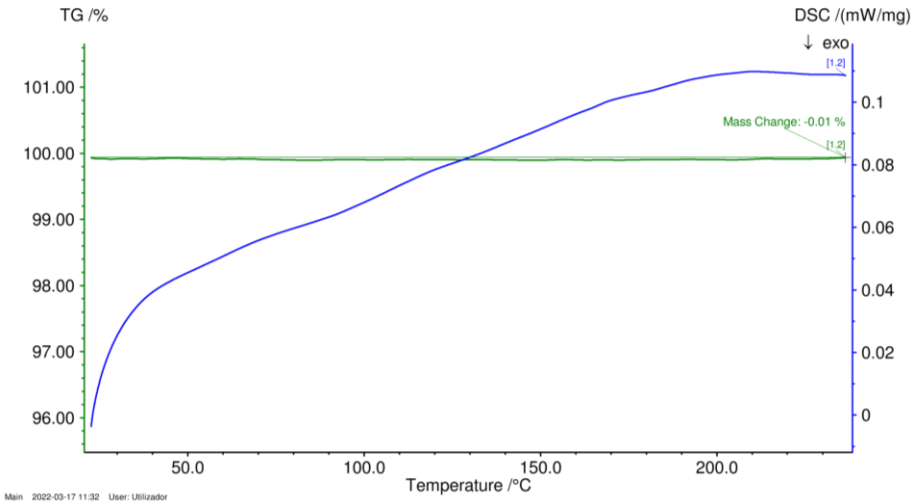

Figure B 2. DSC for sample BT-3µm from 25 ℃ to 220 ℃.

IV. SEM imaging HAp NWs

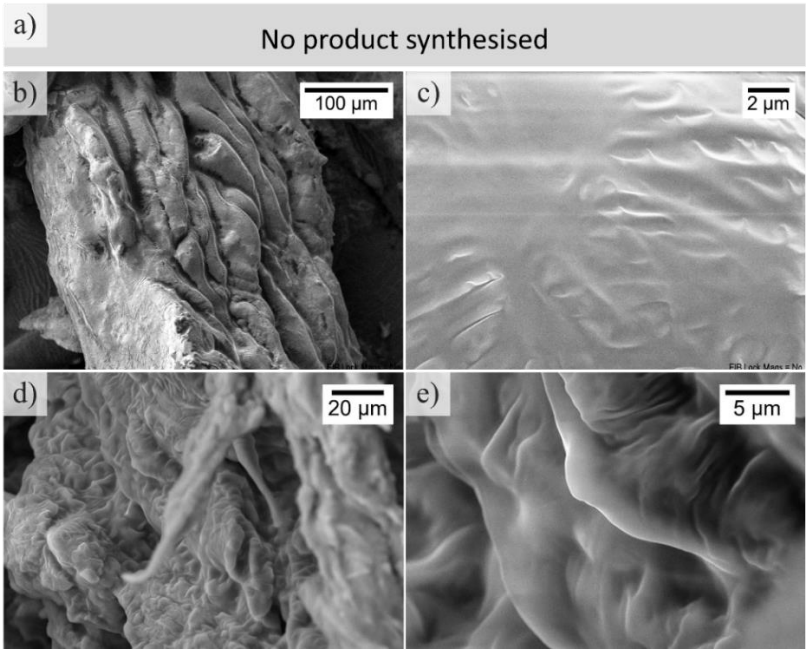

Figure B 3. SEM imaging of Hydroxyapatite synthesized at 120ºC for a) 18hours, b) and c) 24 hours and d) and e) 30 hours.

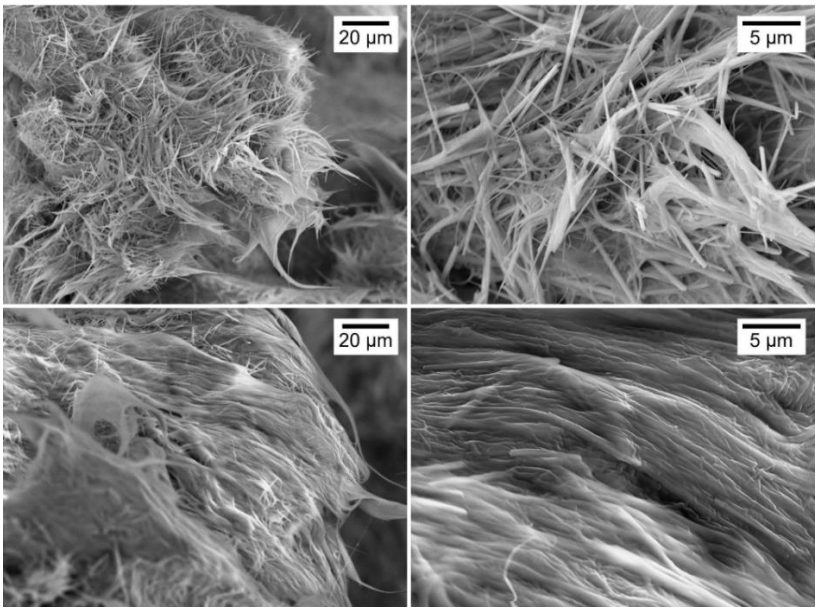

Figure B 4. SEM imaging of Hydroxyapatite synthesized for 180ºC for 18 hours.

V. Calculation of the aerogel porosity

D=3,16g/cm^3 is the theoretical density of hydroxyapatite
r=0,75cm is the radius of the aerogel
h=3mm is the height of the aerogel
Aerogel volume = $\pi r^2 \times h$ = 0,53 cm^3

Expected weight = $D \times$ Aerogel volume= 1,6748g

Porosity is given by $P(\%)=\frac{RW}{EW}\times 100$

Table B 1. Porosity of the fabricated HAp and HAp/BT samples and replicas.

Sample name	HAp	HAp	HAp	HAp	HAp/BT 280	HAp/BT 280	HAp/BT 280
Real weight (mg)	6.00	5.90	5.80	5.00	5.00	5.40	5.10
Porosity (%)	99.64	99.65	99.65	99.70	99.70	99.68	99.70
Sample name	HAp/BT2	HAp/BT2	HAp/BT2	HAp/BT3	HAp/BT3	HAp/BT3	Average
Real weight (mg)	5.40	4.90	5.20	5.00	5.40	5.4	5.35
Porosity (%)	99.68	99.71	99.69	99.70	99.68	99.68	9.68

VI. Cytotoxicity assays

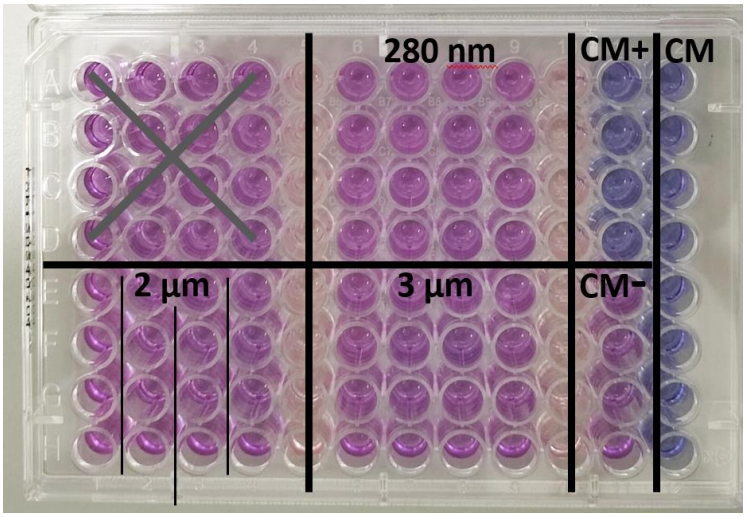

Figure B 5. Sample distribution along the plate for cytotoxicity assays of $BaTiO_3$, sizes 280 nm, 2 µm, 3 µm and of negative (CM-) and positive (CM+) control groups, after the addition of resazurin.

Table B 2. Relative population of Vero cells on cytotoxicity tests of $BaTiO_3$ particles for different dilution factors.

	Relative cell population (%)				**Relative uncertainty of the cell population (%)**			
Dilution	50mg/ml	25mg/ml	12,5mg/ml	6,25mg/ml	50mg/ml	25mg/ml	12,5mg/ml	6,25mg/ml
280nm	111	109	104	107	9	8	6	5
2µm	106	103	106	105	4	3	7	8
3µm	113	114	114	113	7	4	3	4

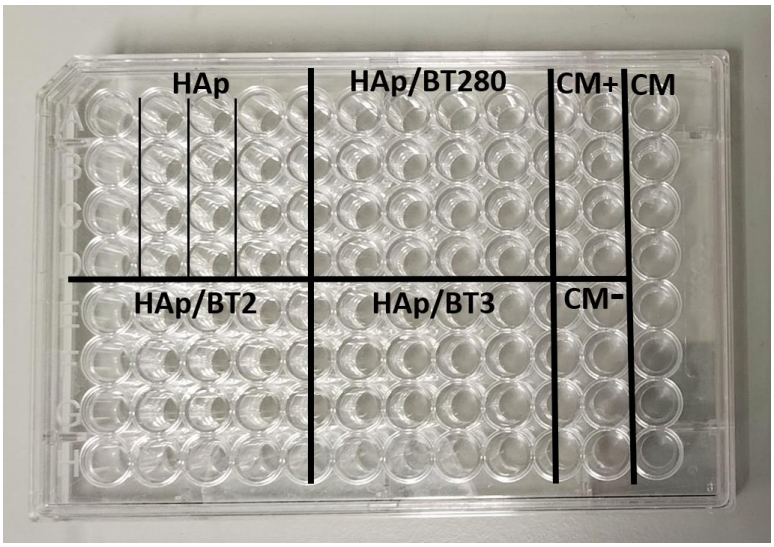

Figure B 6. Sample distribution along the plate for cytotoxicity assays of HAp, HAp/BT280, HAp/BT2 and HAp/BT3 and of negative (CM-) and positive (CM+) control groups.

Table B 3. Relative population of Vero cells on cytotoxicity tests of HAp, HAp/BT280, HAp/BT2 and HAp/BT3 aerogels for different dilution factors.

	Relative cell population (%)				**Relative uncertainty of the cell population (%)**			
Dilution	1mg/ml	0,5mg/ml	0,25mg/ml	0,075mg/ml	1mg/ml	0,5mg/ml	0,25mg/ml	0,075mg/ml
HAp	10	144	147	126	2	14	13	15
HAp/BT280	66	140	138	126	9	10	14	9
HAp/BT2	55	143	138	121	3	18	16	14
HAp/BT3	36	150	136	127	13	7	20	17

VII. Bioactivity assays – SBF submersion

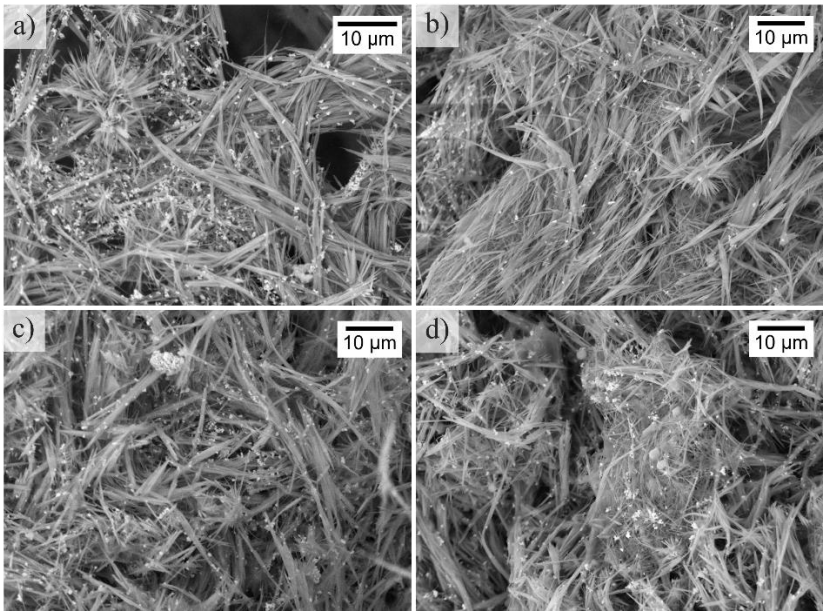

Figure B 7. SEM images of HAp/BT280 aerogel a) with no days in SBF, b) after 1 day in SBF, c) after 3 days in SBF and d) after 7 days in SBF.

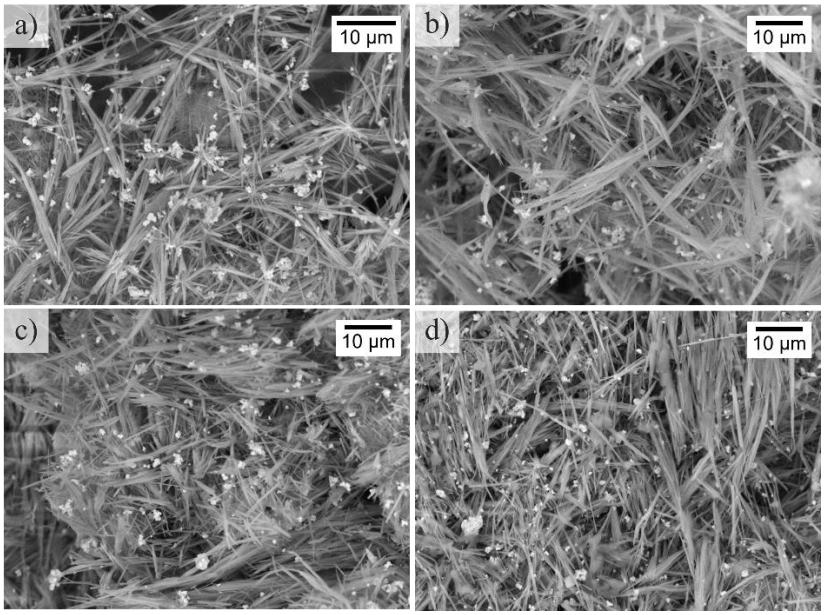

Figure B 8. SEM images of HAp/BT2 aerogel a) with no days in SBF, b) after 1 day in SBF, c) after 3 days in SBF and d) after 7 days in SBF.

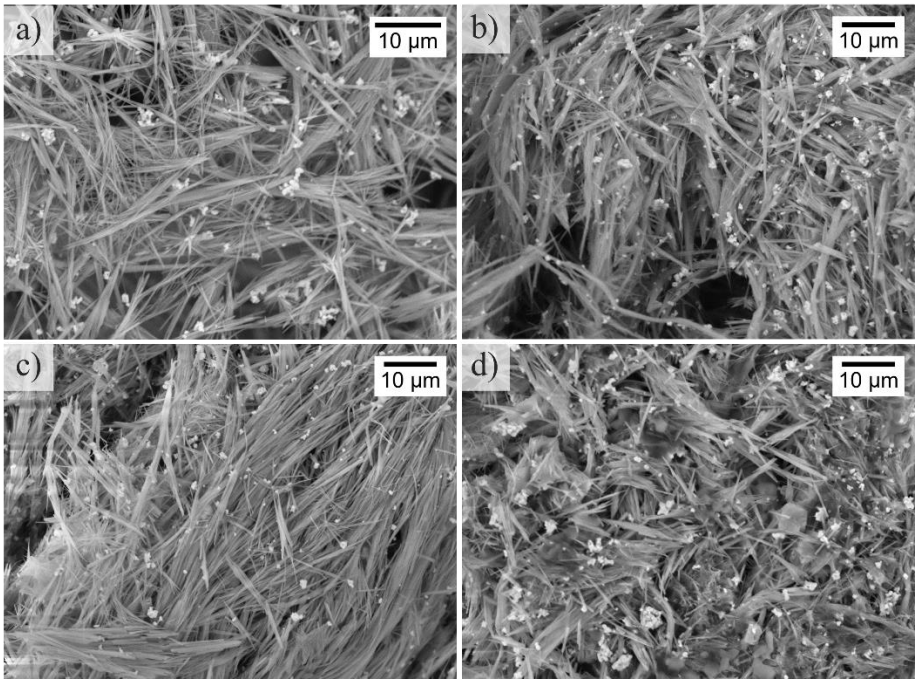

Figure B 9. SEM images of HAp/BT3 aerogel a) with no days in SBF, b) after 1 day in SBF, c) after 3 days in SBF and d) after 7 days in SBF.

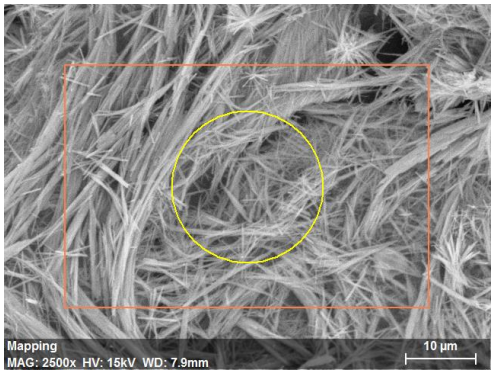

Spectrum: Point

Element	AN	Series	Net unn. C [wt.%]	norm. C [wt.%]	Atom. C [at.%]
Oxygen	8	K-series	1436	24.98	28.65	41.72
Calcium	20	K-series	16813	35.60	40.83	23.74
Carbon	6	K-series	533	8.49	9.74	18.90
Phosphorus	15	K-series	11483	18.12	20.78	15.64
Titanium	22	K-series	0	0.00	0.00	0.00
Barium	56	L-series	0	0.00	0.00	0.00
		Total:		87.20	100.00	100.00

Figure B 10. Quantifying EDS analysis of the HAp aerogel, control sample not immersed in SBF.

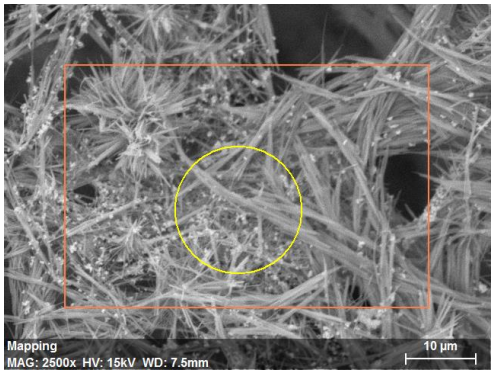

Spectrum: Point

Element	AN	Series	Net unn. C [wt.%]	norm. C [wt.%]	Atom. C [at.%]
Oxygen	8	K-series	1110	22.26	26.52	42.52
Calcium	20	K-series	9734	27.61	32.89	21.05
Phosphorus	15	K-series	6432	16.38	19.51	16.16
Carbon	6	K-series	339	6.29	7.49	16.00
Titanium	22	K-series	974	4.15	4.94	2.65
Barium	56	L-series	1276	7.26	8.65	1.62
		Total:		83.95	100.00	100.00

Figure B 11. Quantifying EDS analysis of the HAp/BT280 aerogel, control sample not immersed in SBF.

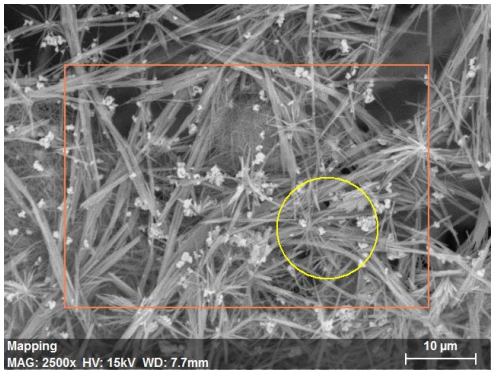

Spectrum: Point

Element	AN	Series	Net	unn. C [wt.%]	norm. C [wt.%]	Atom. C [at.%]
Oxygen	8	K-series	347	12.51	17.98	34.55
Calcium	20	K-series	5533	26.81	38.54	29.56
Phosphorus	15	K-series	3370	14.89	21.40	21.24
Carbon	6	K-series	65	2.09	3.01	7.70
Titanium	22	K-series	610	4.47	6.42	4.12
Barium	56	L-series	897	8.80	12.65	2.83
			Total:	69.57	100.00	100.00

Figure B 12. Quantifying EDS analysis of the HAp/BT2 aerogel, control sample not immersed in SBF.

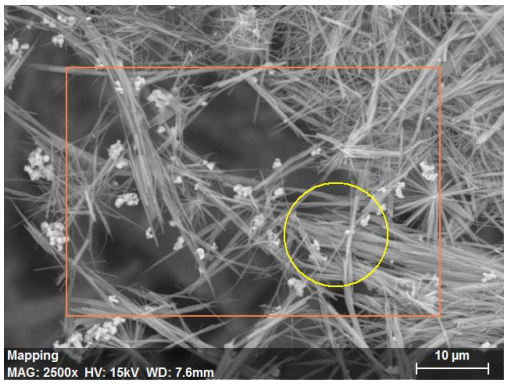

Spectrum: Point

Element	AN	Series	Net	unn. C [wt.%]	norm. C [wt.%]	Atom. C [at.%]
Oxygen	8	K-series	461	19.33	25.52	43.06
Calcium	20	K-series	5505	30.47	40.23	27.10
Phosphorus	15	K-series	3053	14.22	18.77	16.36
Carbon	6	K-series	89	3.20	4.23	9.51
Titanium	22	K-series	461	3.61	4.77	2.69
Barium	56	L-series	467	4.91	6.48	1.27
			Total:	75.74	100.00	100.00

Figure B 13. Quantifying EDS analysis of the HAp/BT3 aerogel, control sample not immersed in SBF.

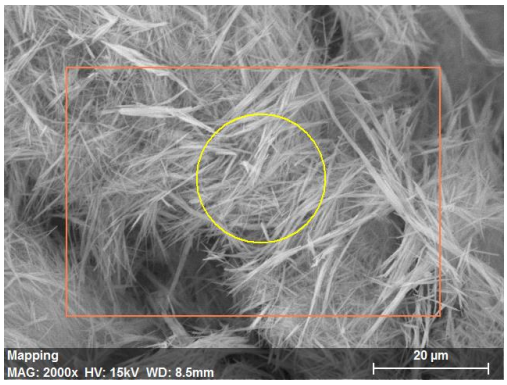

Spectrum: Point

Element	AN	Series	Net	unn. C [wt.%]	norm. C [wt.%]	Atom. C [at.%]
Oxygen	8	K-series	1149	35.08	39.17	52.02
Carbon	6	K-series	315	9.43	10.53	18.63
Calcium	20	K-series	6721	30.77	34.35	18.21
Phosphorus	15	K-series	4561	13.51	15.09	10.35
Sodium	11	K-series	121	0.76	0.85	0.79
Chlorine	17	K-series	0	0.00	0.00	0.00
Titanium	22	K-series	0	0.00	0.00	0.00
Barium	56	L-series	0	0.00	0.00	0.00
			Total:	89.56	100.00	100.00

Figure B 14.Quantifying EDS analysis of the HAp aerogel after 1 day in SBF.

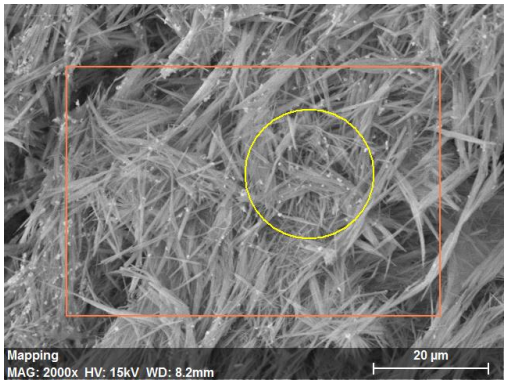

Spectrum: Point

Element	AN	Series	Net	unn. C [wt.%]	norm. C [wt.%]	Atom. C [at.%]
Oxygen	8	K-series	1314	42.18	42.03	54.04
Carbon	6	K-series	326	12.01	11.96	20.49
Calcium	20	K-series	4932	29.41	29.30	15.04
Phosphorus	15	K-series	3578	10.72	10.69	7.10
Sodium	11	K-series	270	1.49	1.48	1.33
Chlorine	17	K-series	672	2.22	2.21	1.28
Titanium	22	K-series	166	1.35	1.34	0.58
Barium	56	L-series	91	0.99	0.99	0.15
Total:				100.36	100.00	100.00

Figure B 15. Quantifying EDS analysis of the HAp/BT280 aerogel after 1 day in SBF.

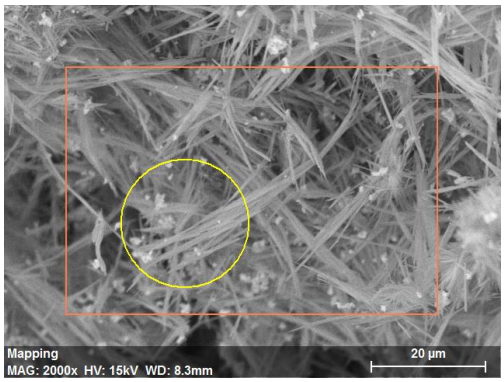

Spectrum: Point

Element	AN	Series	Net	unn. C [wt.%]	norm. C [wt.%]	Atom. C [at.%]
Oxygen	8	K-series	1746	38.77	45.72	60.23
Carbon	6	K-series	300	7.39	8.71	15.29
Calcium	20	K-series	4760	21.62	25.50	13.41
Phosphorus	15	K-series	3408	9.66	11.39	7.75
Titanium	22	K-series	458	2.46	2.90	1.28
Sodium	11	K-series	172	1.03	1.22	1.12
Barium	56	L-series	472	3.42	4.03	0.62
Chlorine	17	K-series	137	0.45	0.53	0.31
Total:				84.79	100.00	100.00

Figure B 16. Quantifying EDS analysis of the HAp/BT2 aerogel after 1 day in SBF.

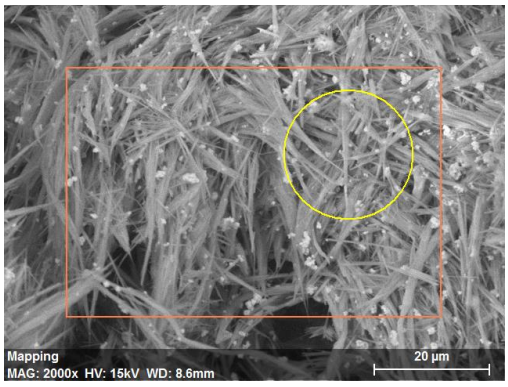

Spectrum: Point

Element	AN	Series	Net	unn. C [wt.%]	norm. C [wt.%]	Atom. C [at.%]
Oxygen	8	K-series	1168	33.90	41.59	53.68
Carbon	6	K-series	302	9.80	12.02	20.66
Calcium	20	K-series	3953	19.81	24.30	12.52
Phosphorus	15	K-series	2599	9.03	11.08	7.39
Sodium	11	K-series	280	2.26	2.77	2.49
Chlorine	17	K-series	593	2.47	3.03	1.76
Titanium	22	K-series	310	2.08	2.55	1.10
Barium	56	L-series	243	2.18	2.68	0.40
Total:				81.53	100.00	100.00

Figure B 17. Quantifying EDS analysis of the HAp/BT3 aerogel after 1 day in SBF.

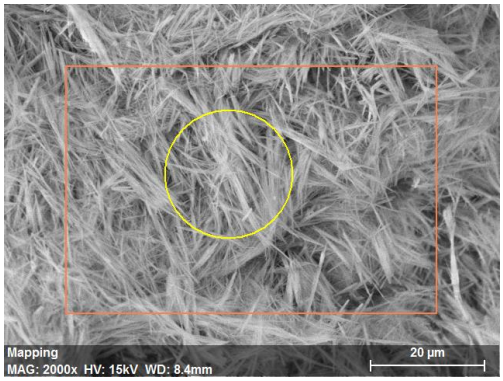

Spectrum: Point

Element	AN	Series	Net	unn. C [wt.%]	norm. C [wt.%]	Atom. C [at.%]
Oxygen	8	K-series	234	16.82	22.22	35.72
Calcium	20	K-series	5502	41.35	54.61	35.04
Carbon	6	K-series	121	5.87	7.75	16.59
Phosphorus	15	K-series	1866	10.56	13.95	11.58
Chlorine	17	K-series	169	1.11	1.47	1.07
Sodium	11	K-series	0	0.00	0.00	0.00
Titanium	22	K-series	0	0.00	0.00	0.00
Barium	56	L-series	0	0.00	0.00	0.00
			Total:	75.72	100.00	100.00

Figure B 18. Quantifying EDS analysis of the HAp aerogel after 3 days in SBF.

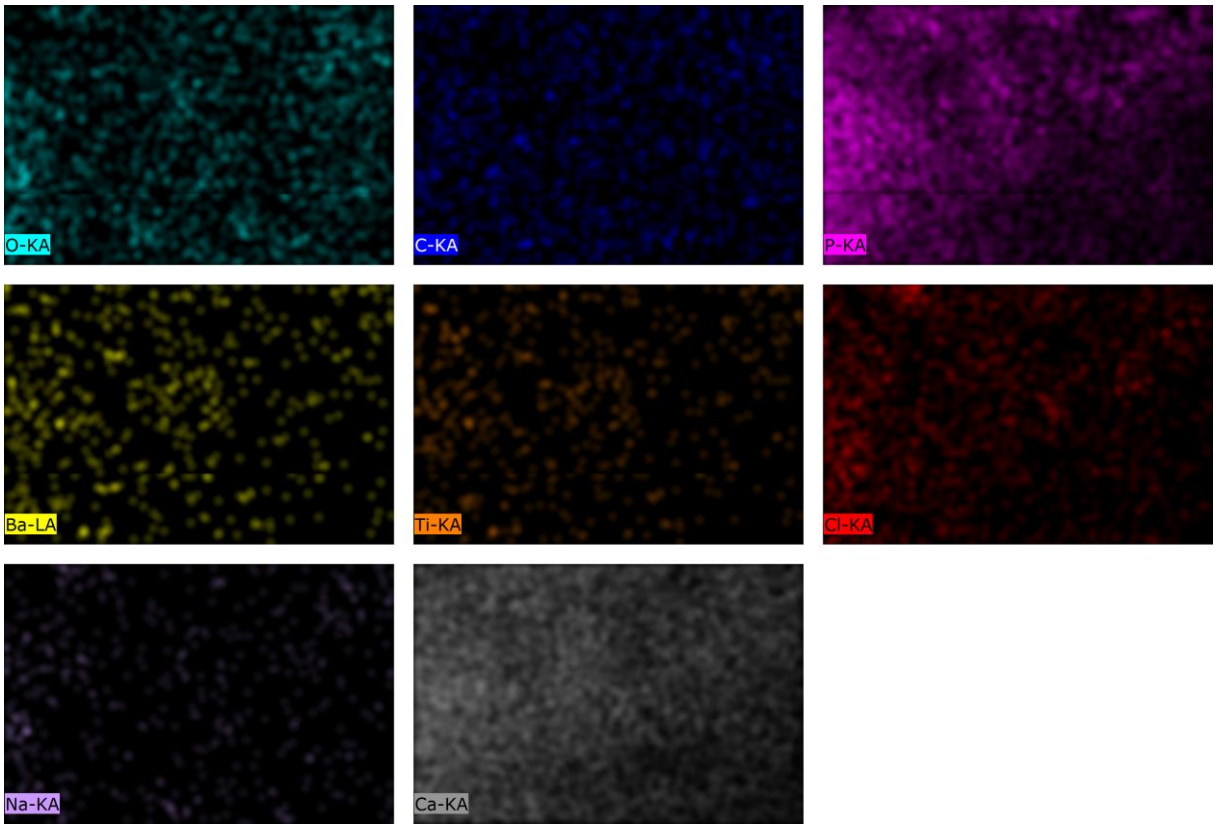

Figure B 19. Mapping EDS analysis of the HAp aerogel after 3 days in SBF.

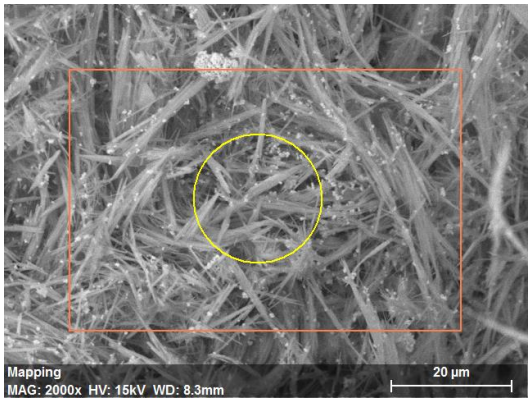

Spectrum: Point

Element	AN	Series	Net	unn. C [wt.%]	norm. C [wt.%]	Atom. C [at.%]
Oxygen	8	K-series	518	13.91	28.02	45.68
Calcium	20	K-series	5454	20.37	41.03	26.70
Carbon	6	K-series	120	2.82	5.69	12.35
Phosphorus	15	K-series	2595	5.81	11.69	9.85
Titanium	22	K-series	406	2.52	5.08	2.77
Chlorine	17	K-series	375	0.95	1.91	1.41
Barium	56	L-series	394	3.26	6.57	1.25
Sodium	11	K-series	0	0.00	0.00	0.00
			Total:	49.65	100.00	100.00

Figure B 20. Quantifying EDS analysis of the HAp/BT280 aerogel after 3 days in SBF.

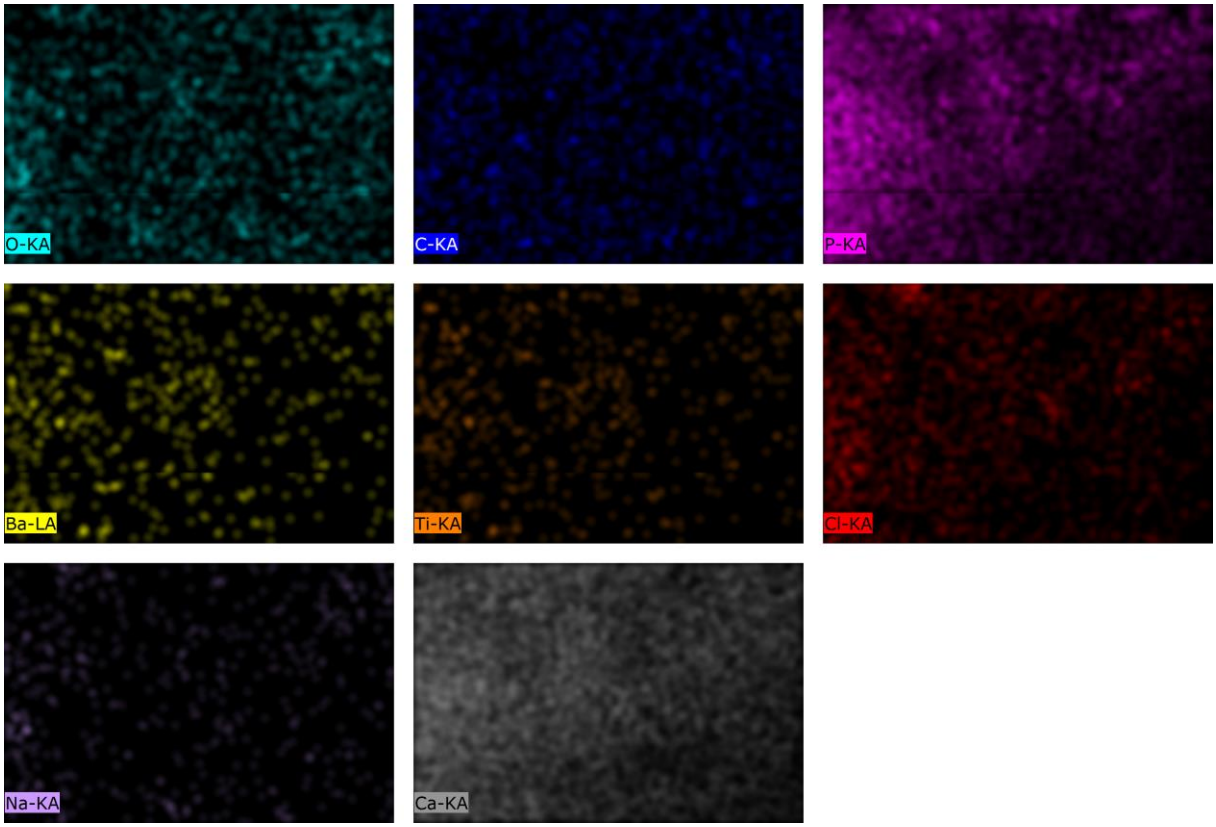

Figure B 21. Mapping EDS analysis of the HAp/BT2 aerogel after 3 days in SBF.

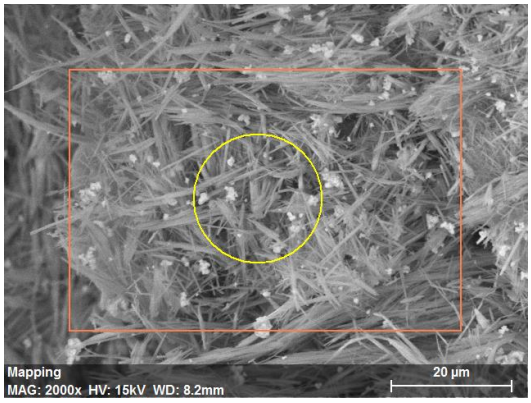

Spectrum: Point

Element	AN	Series	Net	unn. C [wt.%]	norm. C [wt.%]	Atom. C [at.%]
Oxygen	8	K-series	139	25.67	29.60	45.33
Calcium	20	K-series	1646	40.87	47.12	28.81
Carbon	6	K-series	71	7.69	8.86	18.08
Phosphorus	15	K-series	337	5.82	6.71	5.31
Titanium	22	K-series	96	2.83	3.26	1.67
Barium	56	L-series	97	3.86	4.45	0.79
Sodium	11	K-series	0	0.00	0.00	0.00
Chlorine	17	K-series	0	0.00	0.00	0.00
			Total:	86.74	100.00	100.00

Figure B 22. Quantifying EDS analysis of the HAp/BT2 aerogel after 3 days in SBF.

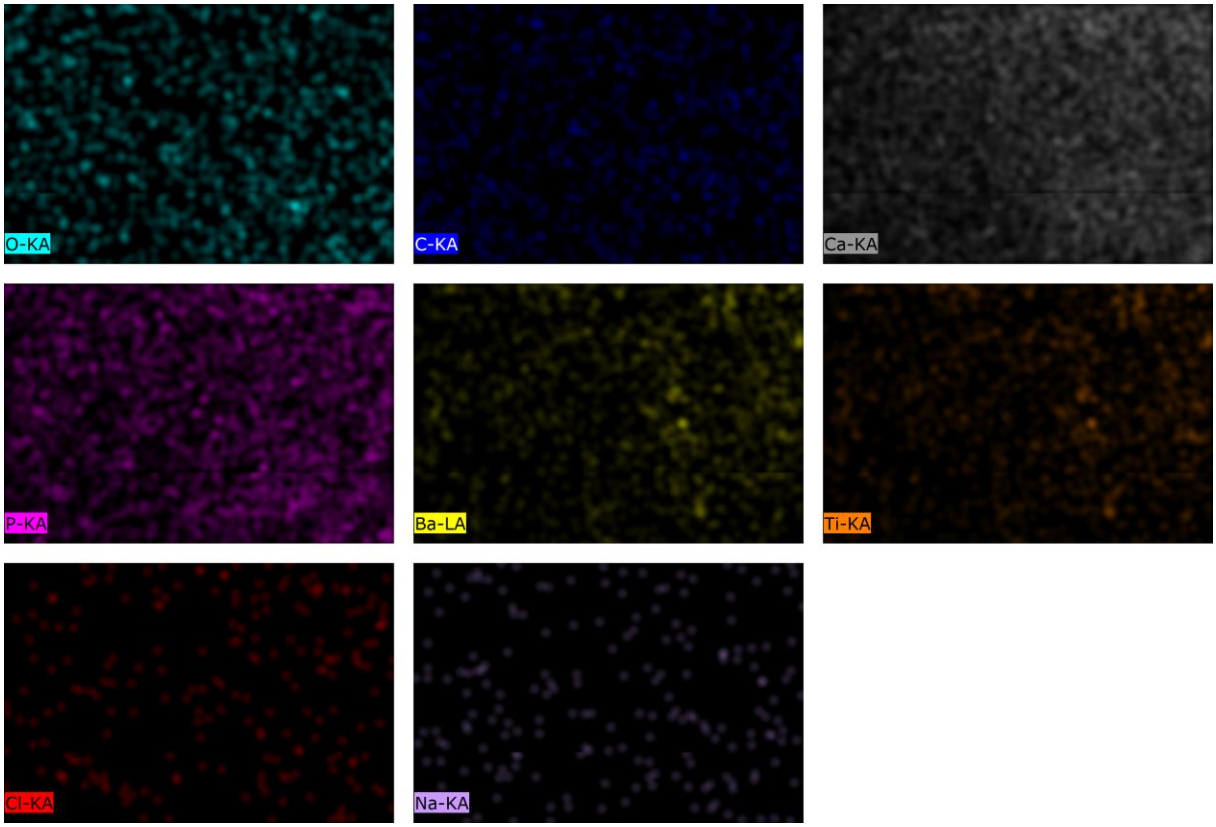

Figure B 23. Mapping EDS analysis of the HAp/BT2 aerogel after 3 days in SBF.

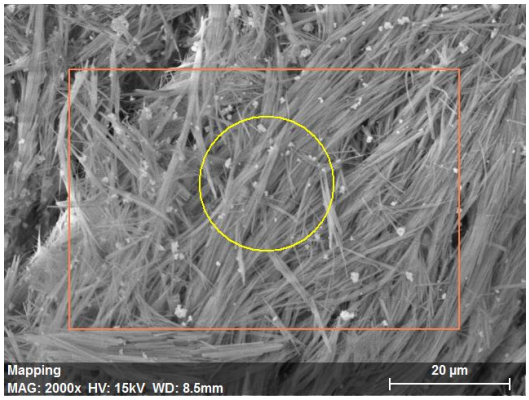

Spectrum: Point

Element	AN	Series	Net	unn. C [wt.%]	norm. C [wt.%]	Atom. C [at.%]
Calcium	20	K-series	3239	33.32	54.15	37.57
Oxygen	8	K-series	141	13.00	21.13	36.73
Phosphorus	15	K-series	928	8.13	13.21	11.85
Carbon	6	K-series	53	3.02	4.91	11.37
Titanium	22	K-series	139	1.85	3.00	1.74
Barium	56	L-series	123	2.21	3.59	0.73
Sodium	11	K-series	0	0.00	0.00	0.00
Chlorine	17	K-series	0	0.00	0.00	0.00
			Total:	61.53	100.00	100.00

Figure B 24. Quantifying EDS analysis of the HAp/BT3 aerogel after 3 days in SBF.

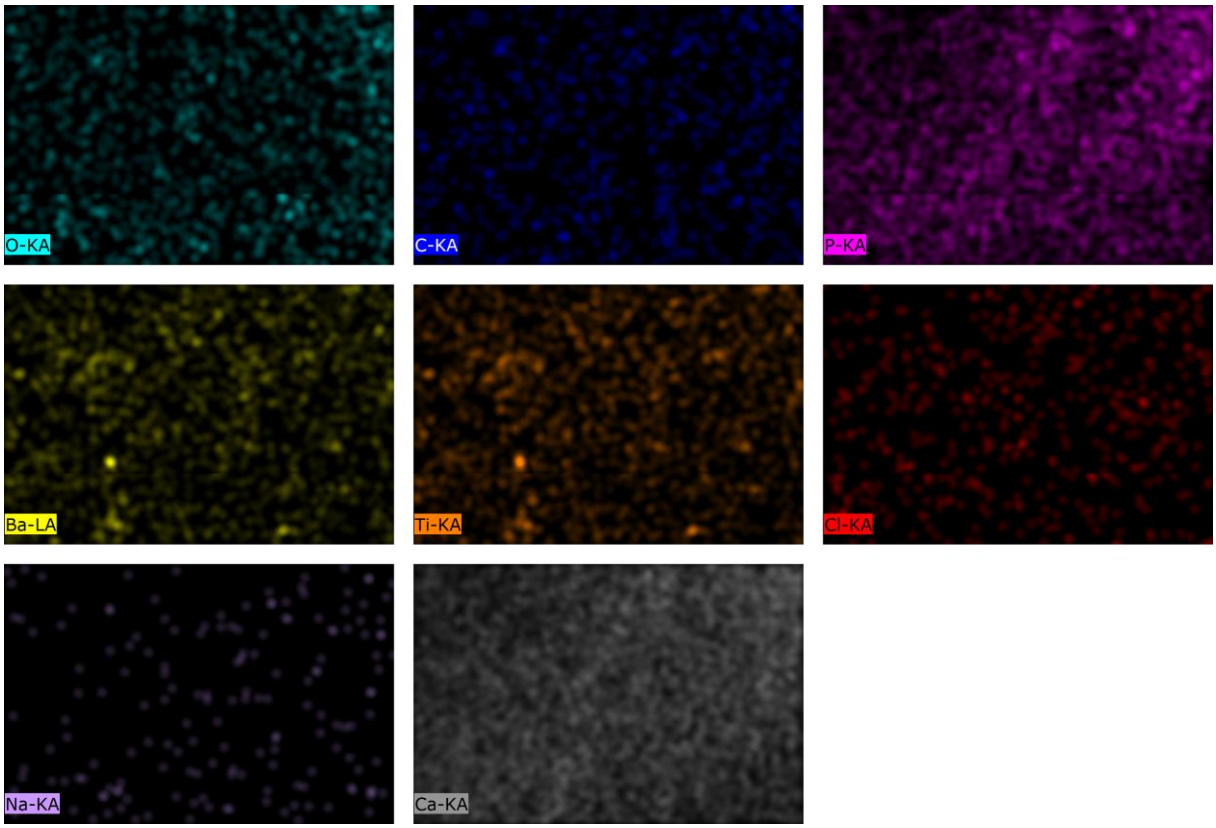

Figure B 25. Mapping EDS analysis of the HAp/BT3 aerogel after 3 days in SBF.

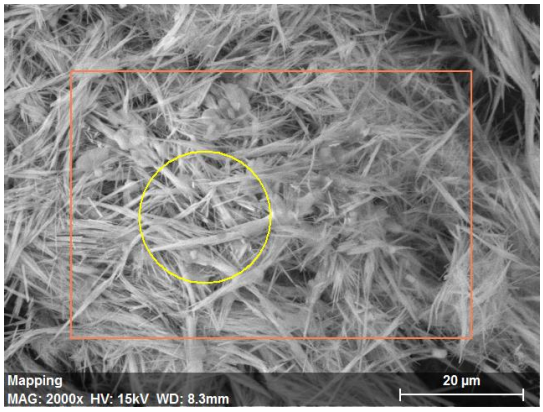

Spectrum: Point

Element	AN	Series	Net	unn. C [wt.%]	norm. C [wt.%]	Atom. C [at.%]
Oxygen	8	K-series	736	34.80	38.72	48.99
Carbon	6	K-series	233	13.33	14.83	24.99
Calcium	20	K-series	3276	25.74	28.63	14.46
Phosphorus	15	K-series	2115	9.09	10.11	6.61
Chlorine	17	K-series	1060	5.31	5.91	3.38
Sodium	11	K-series	183	1.61	1.79	1.57
Titanium	22	K-series	0	0.00	0.00	0.00
Barium	56	L-series	0	0.00	0.00	0.00
			Total:	89.89	100.00	100.00

Figure B 26. Quantifying EDS analysis of the HAp aerogel after 7 days in SBF.

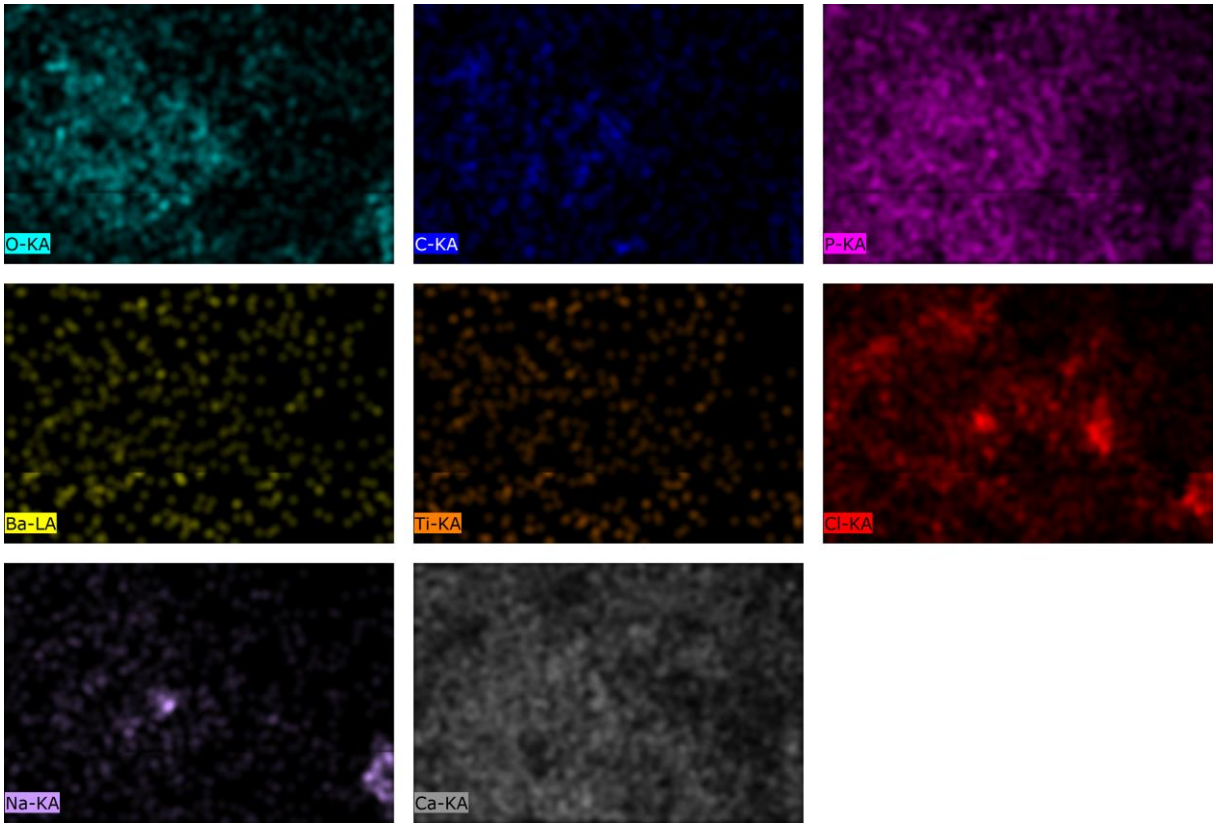

Figure B 27. Mapping EDS analysis of the HAp/BT280 aerogel after 7 days in SBF.

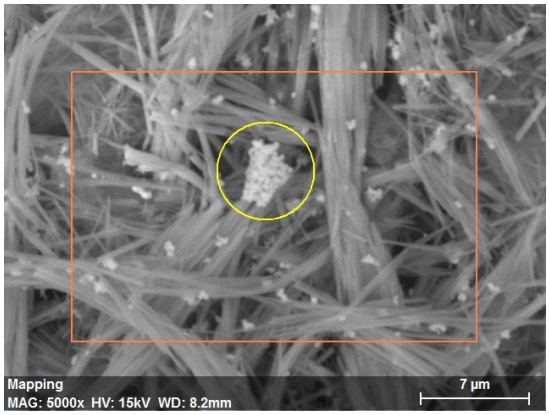

Spectrum: Point

Element	AN	Series	Net	unn. C [wt.%]	norm. C [wt.%]	Atom. C [at.%]
Oxygen	8	K-series	525	26.85	33.44	49.89
Carbon	6	K-series	115	7.34	9.14	18.17
Calcium	20	K-series	1719	16.59	20.66	12.30
Phosphorus	15	K-series	1234	7.42	9.25	7.12
Titanium	22	K-series	394	5.97	7.43	3.71
Chlorine	17	K-series	625	4.17	5.19	3.50
Sodium	11	K-series	163	2.54	3.16	3.28
Barium	56	L-series	465	9.41	11.72	2.04
			Total:	80.29	100.00	100.00

Figure B 28. Quantifying EDS analysis of the HAp/BT280 aerogel after 7 days in SBF.

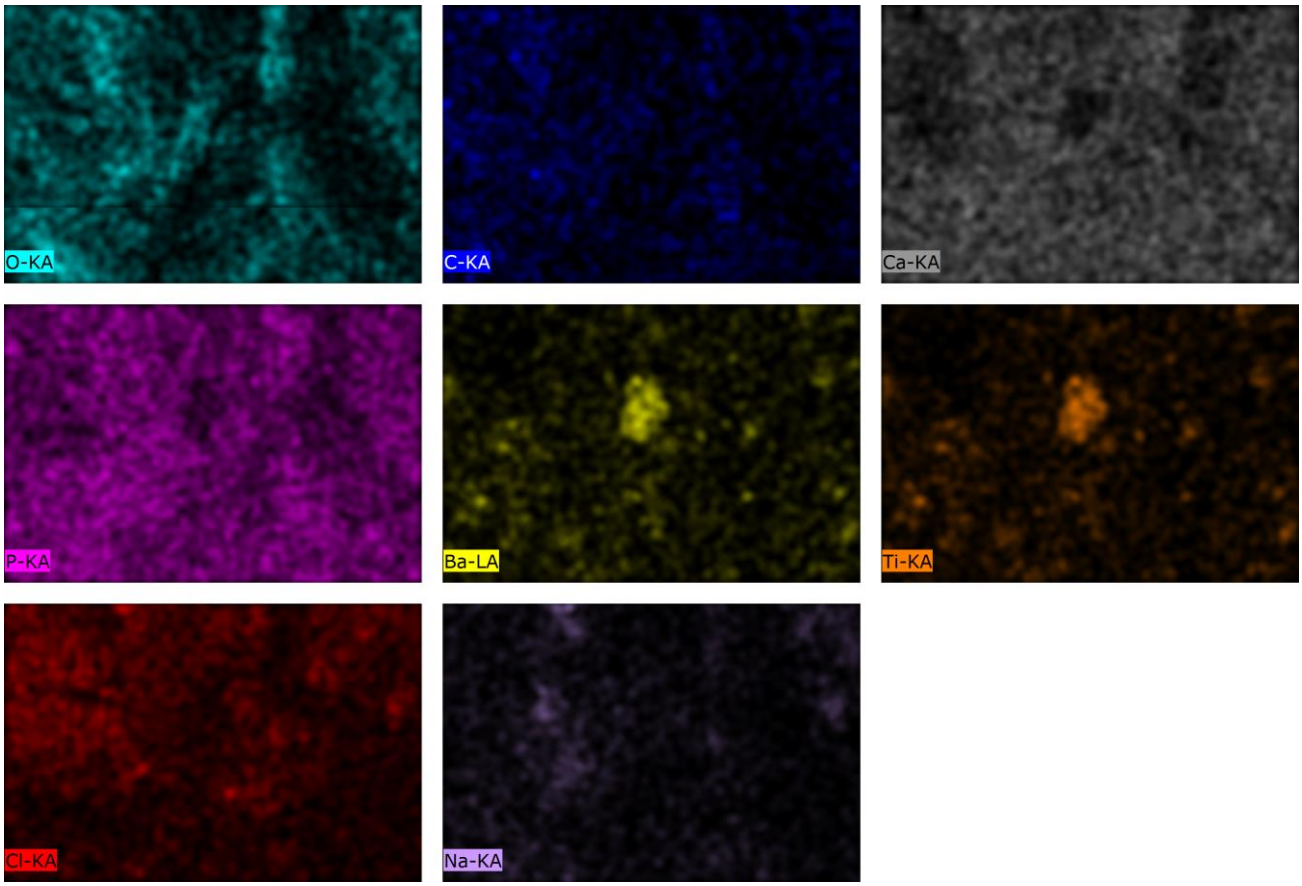

Figure B 29. Mapping EDS analysis of the HAp/BT280 aerogel after 7 days in SBF.

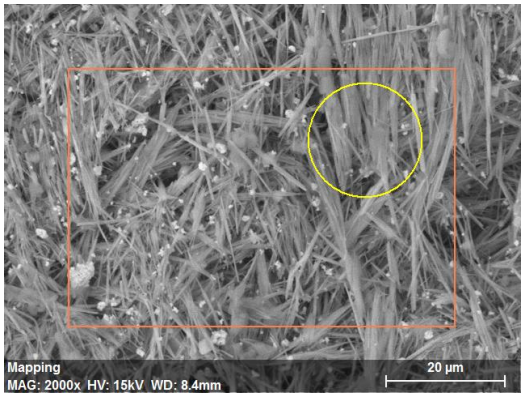

Spectrum: Point

Element	AN	Series	Net unn. C [wt.%]	norm. C [wt.%]	Atom. C [at.%]
Oxygen	8	K-series	1201	37.36	40.37	54.09
Carbon	6	K-series	259	9.33	10.09	18.00
Calcium	20	K-series	4544	25.45	27.50	14.71
Phosphorus	15	K-series	3064	10.23	11.06	7.65
Chlorine	17	K-series	813	3.14	3.39	2.05
Sodium	11	K-series	268	1.86	2.01	1.87
Titanium	22	K-series	326	2.40	2.60	1.16
Barium	56	L-series	280	2.76	2.99	0.47
		Total:		92.52	100.00	100.00

Figure B 30. Quantifying EDS analysis of the HAp/BT2 aerogel after 7 days in SBF.

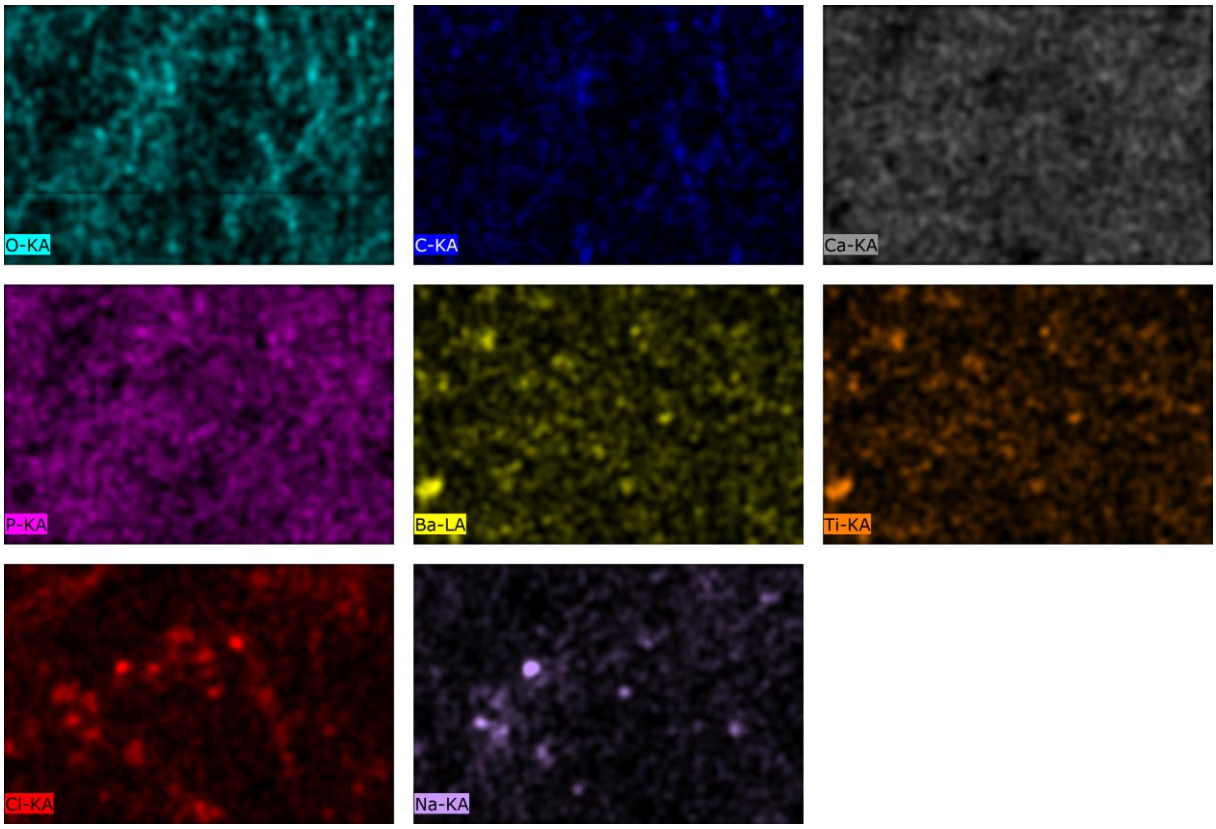

Figure B 31. Mapping EDS analysis of the HAp/BT2 aerogel after 7 days in SBF.

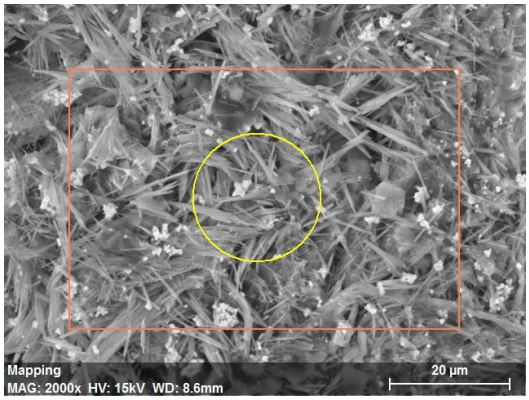

Spectrum: Point

Element	AN	Series	Net	unn. C [wt.%]	norm. C [wt.%]	Atom. C [at.%]
Oxygen	8	K-series	812	25.38	33.64	44.06
Carbon	6	K-series	301	12.13	16.08	28.06
Calcium	20	K-series	3104	13.06	17.31	9.05
Phosphorus	15	K-series	2155	8.63	11.43	7.74
Chlorine	17	K-series	1747	9.26	12.27	7.25
Sodium	11	K-series	183	1.56	2.07	1.89
Titanium	22	K-series	336	2.27	3.00	1.31
Barium	56	L-series	353	3.17	4.20	0.64
Total:				75.44	100.00	100.00

Figure B 32. Quantifying EDS analysis of the HAp/BT3 aerogel after 7 days in SBF.

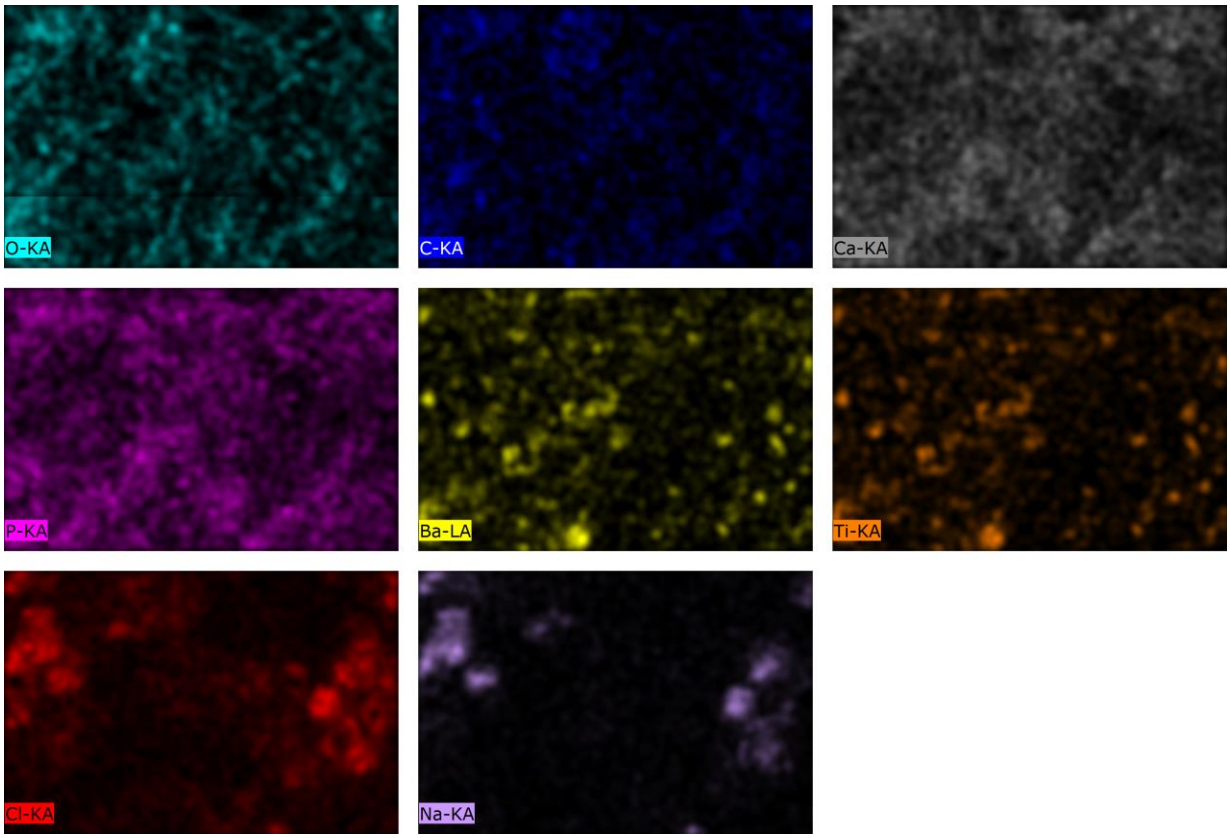

Figure B 33. Mapping EDS analysis of the HAp/BT3 aerogel after 7 days in SBF.